Highlights

MonteCarlo Biphasic Estimation of Fire Properties (McBEF): Part II, Night-time VIIRS Implementation

Meng Zhou, Arlindo M. da Silva, Jun Wang, David A. Peterson

- Applied McBEF to global VIIRS data for sub-pixel fire property retrievals
- Retrieved phase-specific temperature shows biome-dependent global patterns
- McBEF reduces FRP uncertainty and corrects angular dependence artifacts
- Flaming temperature correlates strongly with fire weather index in Australia
- PyroCb events show elevated flaming heat flux in McBEF retrievals

MonteCarlo Biphasic Estimation of Fire Properties (McBEF): Part II, Night-time VIIRS Implementation

Meng Zhou[a,b], Arlindo M. da Silva[b], Jun Wang[c], David A. Peterson[d]

[a] *Goddard Earth Sciences Technology and Research II, Baltimore, University of Maryland, , Baltimore, 21228, MD, USA*
[b] *Global Modeling and Assimilation Office, NASA Goddard Space Flight Center, , Greenbelt, 20771, MD, USA*
[c] *Department of Chemical and Biochemical Engineering, University of Iowa, , Iowa City, 52242, IA, USA*
[d] *Marine Meteorology Division, Naval Research Laboratory, , Monterey, 93943, CA, USA*

Abstract

This study presents the application and global evaluation of the Monte Carlo Biphasic Estimation of Fire Properties (McBEF) algorithm using nighttime observations from the Visible Infrared Imaging Radiometer Suite (VIIRS). McBEF extends traditional fire retrieval techniques by partitioning sub-pixel combustion into flaming and smoldering phases, enabling the estimation of phase-specific temperatures and fractional areas through a Bayesian inference framework. Building upon theoretical analyses and simulation-based validation in Part I, we apply McBEF to the NASA's VIIRS Fire Light Detection Algorithm version 2 (FILDA-2) fire detection product and assess its performance using a series of real-world wildfire cases, high-resolution Landsat observations, and multi-angle VIIRS views. We show that McBEF produces physically consistent fire parameter estimates across diverse land cover types and observation geometries. Compared to conventional empirical Fire Radiative Power (FRP) retrievals, McBEF achieves improved radiative closure and significantly reduces angular dependence in FRP estimates, a key advancement for satellite-based emission inventories. Global analyses reveal biome-specific combustion patterns and seasonal variations in flaming temperature, which correlate well with meteorological indicators such as the Fire Weather Index. A proof-of-concept assessment further demonstrates that McBEF-derived flaming heat fluxes for pyroCb events exceed those of general global fires and align with or exceed thresholds used in plume-rise modeling frameworks. These results confirm that McBEF effectively characterizes sub-pixel

combustion properties and enhances the physical interpretability of satellite fire observations. The algorithm shows strong potential for integration into fire weather, air quality, and climate modeling systems, particularly where accurate vertical smoke injection profiles and energy partitioning are critical.

Keywords: Wildfire, sub-pixel characterization, flaming temperature, smoldering temperature, fire radiative power, heat flux, plume rise, Bayesian, retrievals

1. Introduction

Accurate characterization of sub-pixel wildfire properties is vital for improved wildfire monitoring, emissions estimation, and smoke transport modeling. Conventional satellite-based methods predominantly rely on simplified, bulk representations of fire characteristics, such as total fire radiative power (FRP, Wooster et al., 2003) and burned area (Oliva and Schroeder, 2015), limiting their ability to resolve detailed fire dynamics at the sub-pixel scale (Hoffman et al., 2021). Recent advances in remote sensing instrumentation, particularly from sensors such as the Visible Infrared Imaging Radiometer Suite (VIIRS, Schueler et al., 2002; Xiong et al., 2014), the Sea and Land Surface Temperature Radiometer (SLSTR, Wooster et al., 2012; Xiong et al., 2014) and the Meteorological Imager (METimage, Wallner et al., 2017), offer multi-channel fire-sensitive observations capable of capturing more nuanced fire characteristics, thus opening avenues for more refined sub-pixel fire parameter estimation.

To exploit these enhanced observational capabilities, classical sub-pixel fire retrieval methods such as the bi-spectral Dozier method (BSDM, Dozier, 1981) have been extended in several directions. For instance, Peterson et al. (2013) incorporated atmospheric transmittance corrections to mitigate the effects of absorption along the sensor line-of-sight, improving the physical consistency of retrieved fire parameters. Separately, (Elvidge et al., 2015) expanded the spectral basis of BSDM by incorporating additional shortwave infrared channels, increasing sensitivity to a broader range of combustion temperatures. While these adaptations enhanced retrieval robustness, they still operated under a mono-phasic assumption—estimating a single effective temperature per pixel–which limits their ability to capture intra-pixel combustion phase heterogeneity. Moreover, practical challenges such as the highly dynamic atmospheric transmittance, particularly due to spatiotem-

poral variability in water vapor content (Peterson and Wang, 2013; Deng et al., 2024), as well as view geometry effects and heterogeneous surface backgrounds (Giglio and Kendall, 2001), continue to introduce uncertainty in retrievals. These factors underscore the need for more physically grounded and adaptable estimation frameworks.

In the first part of this two-paper series, Zhou et al. (2026) introduces the Monte Carlo Biphasic Estimation of Fire Properties (McBEF) algorithm. Using a Bayesian inference framework, McBEF addresses these limitations by retrieving phase-specific fire temperatures and fractional areas using. The algorithm employs a bi-phasic parametric model and samples the posterior solution space using a Markov Chain Monte Carlo (MCMC) approach (Gelman et al., 1995; Hoffman et al., 2014; Posselt, 2013). Observing System Simulation Experiments (OSSEs) demonstrates that McBEF achieves robust radiative closure across a range of fire temperature scenarios and spectral channel combinations. The retrieved sub-pixel temperature and fractional area distributions allow for the physically consistent derivation of key fire properties—such as fire radiative power (FRP, Wooster et al., 2003), visible energy fraction (VEF, Wang et al., 2020a), and convective heat flux (Freitas et al., 2007). These results provide a strong theoretical foundation for applying McBEF to real satellite observations.

In this paper, we implement the McBEF algorithm to real multi-channel fire observations which are available in the VIIRS Fire Light Detection Algorithm version 2 (FILDA-2, Zhou et al., 2023), rigorously validating its performance against high-resolution observational datasets and inter-sensor comparisons. We assess the robustness of the McBEF algorithm in operational scenarios, demonstrating improvements in FRP accuracy, reduced angular dependence, and enhanced capability in distinguishing combustion phases relative to conventional empirical approaches. The remainder of this paper is organized as follows: Section 2 briefly reviews the McBEF algorithm, emphasizing its multi-spectral bi-phasic parametric model. Section 3 introduces the datasets, sensor configurations, essential pre-processing steps for McBEF application, and the McBEF implementation for VIIRS FILDA-2 observations. Section 4 presents case studies and offers a comprehensive assessment of McBEF performance against available high-resolution observations. Section 5 concludes with a summary of the key findings and implications for future wildfire monitoring efforts.

2. McBEF Algorithm Overview

2.1. Multispectral bi-phasic fire model and the Bayesian Framework

As demonstrated in Part I (Zhou et al., 2026), a simple bi-phasic fire parametric model when constrained by informative channels is sufficient to describe spectral characteristics of a fire fire event with moderate to high intra-phase temperature heterogeneity. The retrieved temperature phase and areal fractions are not only able to quantity integral radiative properties such as FRP and VEF, but also possess skill for partitioning heat flux estimates needed to constrain plume rise models. As a brief review, the total top-of-atmosphere (TOA) radiance L for a bi-phasic model can be expressed as:

$$\begin{aligned} L(T_f, T_s, T_b, a_s, a_f, \boldsymbol{\lambda}) = B(T_f, \boldsymbol{\lambda})\, a_f + B(T_s, \boldsymbol{\lambda})\, a_s \\ + B(T_b, \boldsymbol{\lambda})\,(1 - a_f - a_s) \end{aligned} \tag{1}$$

Here, T_b represents the background temperature of the surrounding environment and $\boldsymbol{\lambda}$ is the vector of central wavelengths of interest; a_f and a_s are the fractional area for the flaming and smoldering components of a fire within the field of view of a satellite pixel. The term $B(T, \lambda)$ denotes the TOA radiance at temperature T and a given wavelength λ, defined as:

$$B(T, \lambda) = \frac{\int_0^\infty t(\lambda)\epsilon(\lambda)P(\lambda, T)\Phi(\lambda)d\lambda}{\int_0^\infty \Phi(\lambda)d\lambda} \tag{2}$$

where $P(\lambda, T)$ is the Planck function, $\Phi(\lambda)$ is the sensor spectral response function, $t(\lambda)$ is the atmospheric transmittance, and $\epsilon(\lambda)$ is the emissivity of the emitter.

This bi-phasic model assumes that the fire behaves as a black-body or gray-body emitter and is valid in spectral regions where fire radiance is predominantly governed by Planckian emission.

We employ the chain Monte Carlo (MCMC), a Bayesian estimation framework method algorithm for estimating sub-pixel fire properties (Zhou et al., 2026). The posterior distribution of the fire parameters $\boldsymbol{\theta} = \{T_f, T_s, a_f, a_s\}$ given the observed TOA radiances $L^{\text{obs}}(\boldsymbol{\lambda})$ and the known spectral bands $\boldsymbol{\lambda}$ is given by:

$$p(\boldsymbol{\theta} \mid L^{\text{obs}}(\boldsymbol{\lambda}), \boldsymbol{\lambda}, T_b) = \frac{p\left(L^{\text{obs}}(\boldsymbol{\lambda}) \mid \boldsymbol{\lambda}, T_b; \boldsymbol{\theta}\right)\, p(\boldsymbol{\theta})}{p\left(L^{\text{obs}}(\boldsymbol{\lambda}) \mid \boldsymbol{\lambda}, T_b\right)} \quad \text{with} \quad \boldsymbol{\theta} = \{T_f, T_s, a_f, a_s\} \tag{3}$$

The term $p\left(L^{\text{obs}}(\boldsymbol{\lambda}) \mid \boldsymbol{\lambda}, T_b; \boldsymbol{\theta}\right)$ represents the likelihood, which quantifies the probability of observing the radiances given the model parameters and known wavelengths. The prior distribution $p(\boldsymbol{\theta})$ encodes any pre-existing knowledge or physical constraints on the parameters before incorporating the observational data. The denominator $p\left(L^{\text{obs}}(\boldsymbol{\lambda}) \mid \boldsymbol{\lambda}\right)$ is the marginal likelihood or evidence, serving as a normalization constant to ensure the posterior integrates to one; it is often intractable but not needed for parameter sampling via methods such as MCMC. Additional details can be found in (Zhou et al., 2026).

3. McBEF Algorithm Implementation

Building on the development and validation in Part I (Zhou et al., 2026), which used simulated data, this section details the modifications required for application to real-world observations. Figure 1 presents the procedural flow of the McBEF implementation for VIIRS FILDA-2 multi-channel fire and background radiance data. The workflow begins with sensor-specific configuration (Sections 3.1.1 and 3.1.5) and specification of priors for the Bayesian framework, followed by ingestion of the required datasets: FILDA-2 fire observations (Section 3.1.2), surface emissivity and background-temperature climatology (Section 3.1.3), and static heat-source masks (Section 3.1.4). For each valid detection, McBEF first estimates the background temperature (T_b) and a water-vapor scaling factor from the background mean radiance. The inferred scaling factor is then propagated to the fire parameter estimation. Afterward, sub-pixel fire properties are subsequently estimated, and post-sampling summaries–mean, mode, standard deviation, and 95% highest-density interval (HDI)–are produced. The remainder of this section provides details on sensor and dataset, data pre-processing, and critical estimation steps including the background and water-vapor estimation (Section 3.2.1) and the MCMC-based fire property retrievals (Section 3.2.2).

3.1. Sensor, Datasets, and Data Processing

3.1.1. Visible Infrared Imaging Radiometer Suite (VIIRS)

The Visible Infrared Imaging Radiometer Suite (VIIRS) is the primary imaging instrument onboard the Suomi-NPP and NOAA-20 polar-orbiting satellites, with continued operation planned through the JPSS constellation over the next two decades (Schueler et al., 2002; Xiong et al., 2018). VIIRS

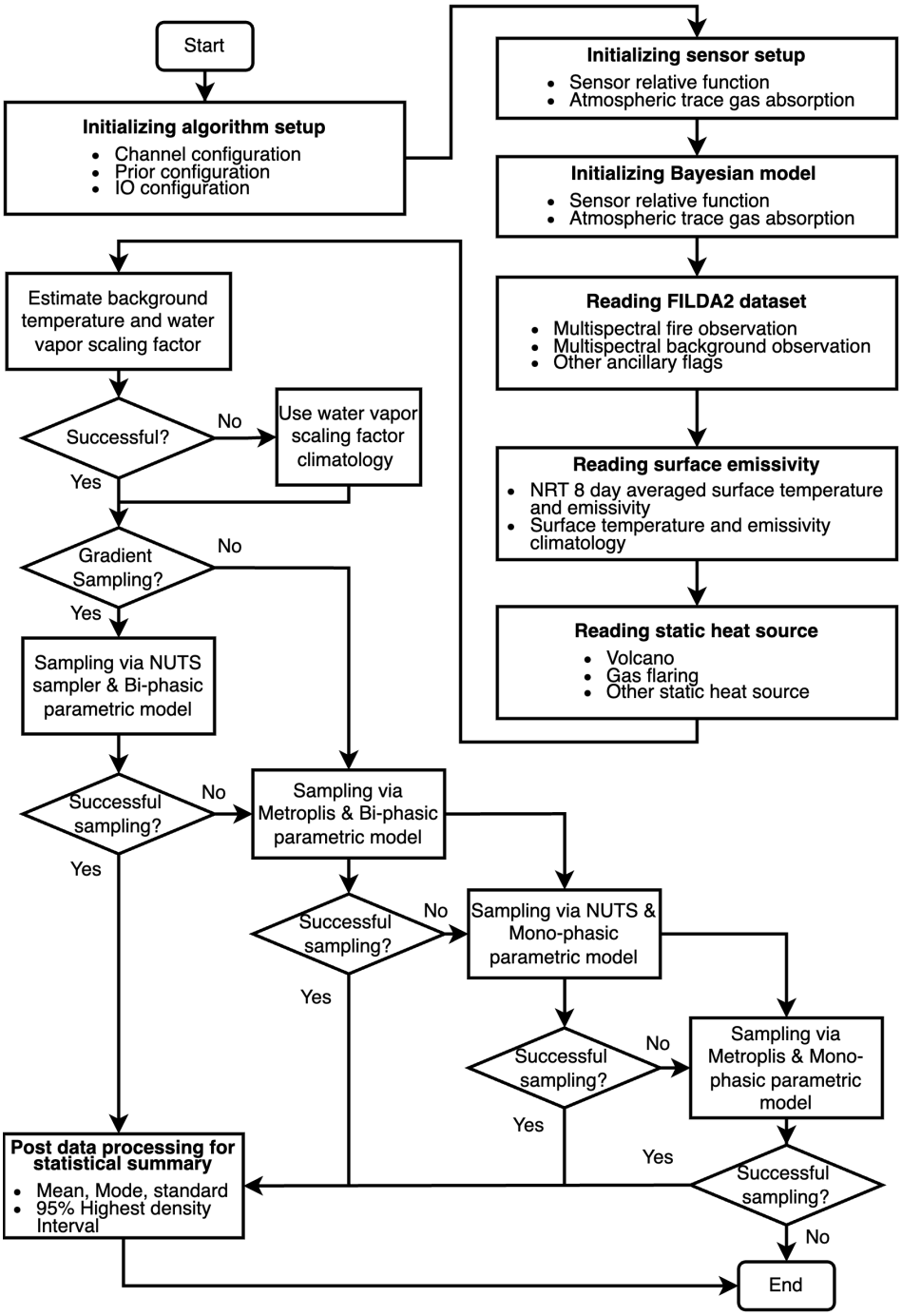

Figure 1: Algorithm flow chart of McBEF implementation for VIIRS FILDA-2

offers 22 spectral bands, including five imagery (I-) bands at 375 m resolution, 16 moderate-resolution (M-) bands at 750 m, and the Day/Night Band (DNB), a highly sensitive panchromatic visible channel capable of detecting low-light signals such as night-time wildfires, city lights, and reflected moonlight (Miller et al., 2013; Zhou et al., 2021, 2024). Compared to predecessors such as MODIS and AVHRR, VIIRS offers several improvements relevant to fire observation: 1. Smaller pixel growth from nadir to edge-of-scan due to onboard aggregation (factor of ∼4, compared to ∼8–10 for MODIS) (Polivka et al., 2015); 2. Multiple nighttime fire-sensitive channels, including SWIR (1.6 and 2.25 μm) and MWIR (3.7, 4.05 μm), enabling improved fire detection and characterization (Elvidge et al., 2013); 3. the unique DNB, which provides visible observations across seven orders of magnitude of radiance (Miller et al., 2013).

This study utilizes VIIRS sensors onboard both the S-NPP (VNP) and NOAA-20 (VJ1) platforms. These satellites are in sun-synchronous polar orbits with nominal 1:30 AM local time equator crossings, offset by ∼50 minutes. Together, they provide complementary nighttime observations of the same fire events under differing view geometries, enabling cross-validation of McBEF retrievals. The relative spectral response (RSR) functions of VIIRS fire-sensitive bands used in this work are obtained from NOAA's Center for Satellite Applications and Research (`https://ncc.nesdis.noaa.gov/VIIRS/VIIRSSpectralResponseFunctions.php`).

3.1.2. FIre Light Detection Algorithm Version 2 (FILDA-2)

The Fire Light Detection Algorithm Version 2 (FILDA-2) is a standard Level 2 fire detection algorithm providing several basic fire properties such as modified combustion efficiency (MCE), FRP and VEF. This is one of the datasets comprising the NASA VIIRS land product suites (Zhou et al., 2023). FILDA-2 integrates the Day/Night Band (DNB), Medium-Wave InfraRed (MWIR), and long wavelength infrared (LWIR) channel radiances, measured by the VIIRS instrument aboard Suomi-NPP (VNP) and NOAA-20/JPSS-1 (VJ1) satellite, to simultaneously improve the fire detection and retrievals of FRP, VEF, and MCE at nighttime. The features and improvements to FILDA-2 include: (a) detection of approximately 25–30% more smaller and cooler fires than the operational VIIRS Active Fire 375m I-band algorithm; (b) retrieval of the MCE for each individual fire event globally every day, enabling the estimation of pixel level emission factors for characterization of wild fire emissions; (c) correction for the impact of atmospheric absorption

on the FRP estimation (Deng et al., 2024), which substantially mitigates the angular dependence of FRP density. The double counting of the fire detection caused by the bow-tie effect of the VIIRS observation is also mitigated by FILDA-2.

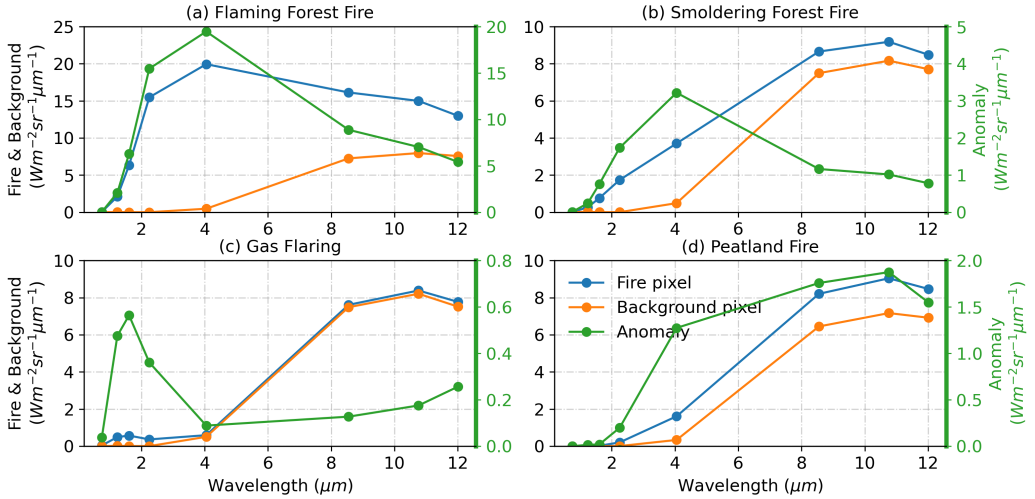

Figure 2: Selected FILDA-2 multi-spectral radiance for detected Thermal anomalies of different types. (a)Flaming forest fire; (b) Smoldering forest fire;(c) gas flaring burning; (d) Peat land burning over Indonesia.

FILDA-2 also provides the multi-spectral radiance of the fire pixel and the background mean radiance across the available VIIRS bands, including the panchromatic DNB (0.5–0.9 μm), M08 (1.24 μm), M10 (1.6 μm), M11(2.25 μm), M13 (4.05 μm), M14 (8.55 μm), M15 (10.5μm), and M16 (12.01 μm). The multi-spectral background radiance is derived through a spatial dynamical window ranging from 4×4 km^2 to 20×20 km^2, with the thermal anomalies and suspicious high temperature pixels removed. Fig. 2 shows examples of the multi-spectral fire radiance that provided by FILDA-2. As shown, the peak of the radiance anomaly of flaming forest fire is shown smaller than 4 μm (Fig. 2a), while for smoldering forest fire, the peak is shown closer or longer than 4 μm (Fig. 2b). Gas flaring, whose temperature is well known to be high, shows a peak of radiance around 1.6 μm. And at last, for a peat land fire over Indonesia, the peak of the radiance is longer the case of the smoldering forest fire. This multi-spectral fire radiance of FILDA-2 enables the implementation of McBEF algorithm for advanced fire sub-pixel characterization. The FLIDA-2 data is available at the NASA's Level-1 and

Atmosphere Archive & Distribution System Distributed Active Archive Center (LAADS DAAC, https://ladsweb.modaps.eosdis.nasa.gov/)

3.1.3. VIIRS Land Surface Temperature/Emissivity

We utilize the S-NPP VIIRS Land Surface Temperature (LST)/Emissivity VNP21A2 to generate the surface emissivity climatology required by the estimation algorithm (Islam et al., 2016). The VNP21A2 can be downloaded from the LAADS DAAC. It is an 8-day composite of diel LST/Emissivity data set projected on 1 kilometer resolution sinusoidal grid. To construct the climatology for a given 8-day composite date (e.g., day 9 of 2019), three years of data (e.g., 2017 to 2019) are used. For each year, the composite from the target day, along with its immediate neighbors (e.g., days 1, 9, and 17), are selected. This yields a total of nine composite files, which are then averaged to produce the climatological mean and standard deviation of selected parameters for that target day, including surface emissivity of band M14 (8.55 μm), M15 (10.5 μm), and M16 (12.01 μm) and the daytime and nighttime LST. The surface emissivity is used in the bi-phasic fire parametric model as the $\epsilon(\lambda)$ term to model the background surface radiance. The mean LST and its standard deviation is used as the prior for the background temperature estimation, which will be detailed section 3.2.1.

3.1.4. Surface static thermal anomaly climatology

As documented in the peer-reviewed literature (Li et al., 2021; Liu et al., 2018), the VIIRS I04 band (3.7 μm)–the primary channel used by the VIIRS active fire product (Schroeder et al., 2014) and by FILDA-2 for fire detection– is also sensitive to anthropogenic thermal sources (e.g., gas flaring, industrial cooling, mining) and to natural static thermal sources (e.g., lava at active volcanoes). Consequently, these sources are routinely detected by both the VIIRS active fire algorithm and FILDA-2. Although FILDA-2 employs a gas-flaring database to flag detections at known flaring sites (Elvidge et al., 2015), this alone is insufficient to screen other industrial sources. Additional filtering is needed because (1) such sources are not the focus of this study; (2) they are often located in urban areas where VIIRS Day/Night Band (DNB) measurements are contaminated by artificial light (Li et al., 2021); and (3) their heating mechanisms and temperature distributions differ from biomass burning, which can induce unexpected behavior in algorithms designed for wildfires.

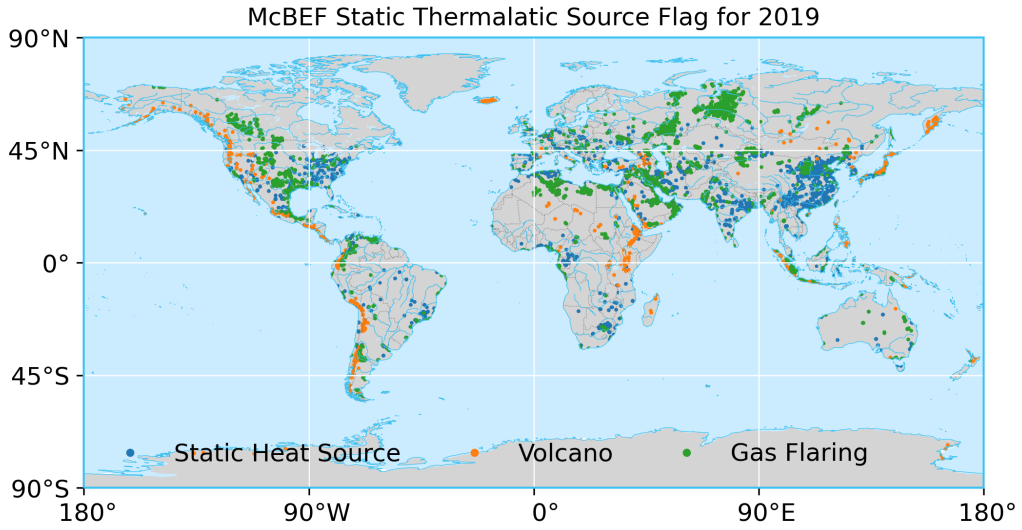

Figure 3: Global static heat source used in McBEF.

To identify persistent non-biomass thermal sources, we perform a frequency analysis using the yearly VIIRS active I-band detections (VNP14IMG and VJ114IMG; hereafter Vxx14IMG) to build a climatology of surface static thermal anomalies. All detections within a year are first remapped to a regular latitude–longitude grid at 0.02° resolution, chosen to be consistent with the nominal 375-m I-band pixel size and a typical off-nadir growth factor of ~ 4. We then aggregate detections by the VIIRS 16-day repeat cycle: within each cycle, if a detection occurs in a grid cell, that cell is assigned a value of one for the cycle; otherwise zero. This yields 23 frames of binary fire-occurrence data per year, which we sum temporally to form an annual per-cycle occurrence count. Grid cells with occurrence counts > 16 cycles are classified as *static heat sources*. This temporal aggregation is preferable to simple annual count thresholds (Li et al., 2021), which can misclassify long-lasting biomass burning (e.g., extended prescribed burns for wasteland reclamation) as spurious anomalies. As illustrated in Fig. A.15a,b, reclamation burns can persist for months and be detected > 40 times in a year, yet they appear in only nine of the 16-day cycles. By contrast, anthropogenic static sources–such as oil and natural–gas facilities (e.g., 9°43′48.0″N, 63°28′12.0″W; Fig. A.15c,d)–are detected in nearly every repeat cycle.

We further augment the static-source mask with volcano locations compiled from the Holocene Volcano List of the Global Volcanism Program

(https://volcano.si.edu/). Figure 3 summarizes the complete set of static heat-source flags used in McBEF. Both the static-source mask and the gas-flaring layer are updated annually and applied to classify detections in the subsequent year.

3.1.5. Atmosphere gas absorption

We use the Unified Linearized Vector Radiative Transfer Model (UNL-VRTM, Wang et al., 2020b), specifically developed for wildfire studies, to calculate line by line atmospheric transmittance $\tau(\lambda)$ and mass extinction coefficients $\alpha(\lambda)$ across the wavelengths of interest. As a first-order approximation, only Rayleigh scattering at standard atmospheric pressure and gas absorption from high-resolution transmission molecular absorption database (HITRAN, Rothman et al., 2013) and Water Vapor Continuum Model (Mlawer et al., 2012) were included. We considered 5 UNL-VRTM build-in standard atmospheric profiles for the calculation(McClatchey, 1972; Wang et al., 2014), including Tropical, Mid-latitude summer, Mid-latitude winter, High-latitude summer, High-latitude winter. Although aerosols such as smoke could further attenuate fire light via scattering and absorption, these complex effects are currently excluded.

3.2. McBEF Implementation based on VIIRS FILDA-2 Data

This section outlines the two sequential steps used to estimate bi-phasic fire properties from VIIRS FILDA-2 multi-channel fire and background radiance observations: (i) estimation of background temperature and a water-vapor scaling factor to accurately account for atmospheric transmittance (Section 3.2.1); and (ii) retrieval of bi-phasic fire properties within an MCMC framework (Section 3.2.2). After accumulating a sufficient number of posterior samples (currently 2,000), McBEF computes post-sampling statistical summaries that provide a robust characterization of the retrieved fire properties. The available output variables are listed in Tables A.3 and A.2.

3.2.1. Surface temperature and water vapor handling

As shown in Eqn. 1, the TOA radiance of a fire pixel, absent solar contamination, consists of both terrestrial background and fire radiance. Accurately estimating the background surface temperature (T_b) is therefore a critical first step in sub-pixel fire characterization. Previous studies have shown that the classic BSDM, which estimates a mono-phasic fire temperature and its

fractional area using 4 μm and 11 μm observations, is highly sensitive to uncertainties in T_b. For example, Giglio and Kendall (2001) demonstrated that errors in T_b estimation can lead to fire temperature errors exceeding 100 K and corresponding fractional area errors of up to 50%. This sensitivity arises from the fact that BSDM is a mathematically determined system with no redundancy, offering little resilience to perturbations in the observed signal, including those introduced by T_b and atmospheric effects.

In traditional BSDM applications and its derivatives, T_b is either estimated iteratively from the fire pixel or approximated from neighboring pixels under the assumption of local temperature homogeneity (Peterson et al., 2013; Eckmann et al., 2009; Menzel et al., 1991). Alternatively, the background radiance may be subtracted directly, with fire properties derived from the radiance anomaly. All of these approaches assume unity atmospheric transmittance at both 4 μm and 11 μm. However, as shown by Peterson and Wang (2013), this assumption can be unrealistic and introduces significant errors in T_b, which subsequently propagate into the retrieval of fire properties.

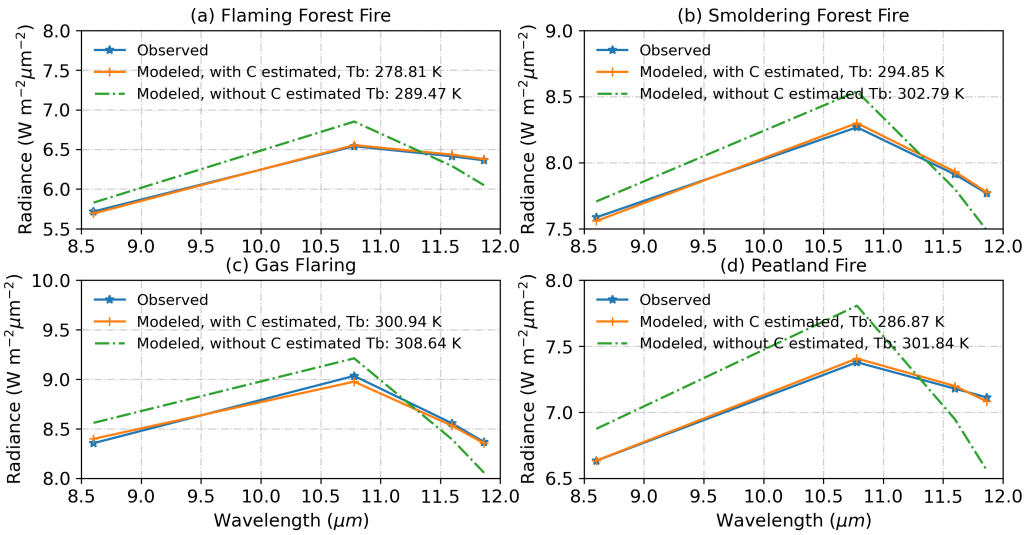

Figure 4: Atmospheric transmittance and gas optical depth at VIIRS band. (a) atmoshperic transmittance at selected VIIRS bands; (b) fractional contribution of the difference atmosphere trace gas to the total optical depth in a aerosol free and standard mid-latitude summer atmosphere profile.

In fact, atmospheric absorption in the mid-wave infrared (MWIR) and thermal infrared (TIR) plays a substantial role in attenuating both fire and

background radiance. Fig. 4 illustrates the atmospheric transmittance and the relative contribution of major absorbing gases to the total optical depth across VIIRS bands, based on the standard mid-latitude summer profile and calculated using UNL-VRTM. Aerosol effects are not considered in this simulation. As shown, for wavelengths beyond 4 μm, atmospheric transmittance generally falls below 70%. Water vapor is the dominant absorber for M14 (8.55 μm), M15 (10.76 μm), and M16 (12.01 μm), contributing over 90% to the total gas optical depth. This attenuation increases at higher view zenith angles due to longer atmospheric path lengths. Moreover, atmospheric water vapor is highly variable, especially in vertical structure and near-surface concentration. In fire-affected regions, total column water vapor is often significantly depleted. For example, Peterson and Wang (2013) observed 40–75% reductions in local column water vapor relative to the mid-latitude summer climatological mean of 2.93 g cm^{-2}.

To address this challenge, McBEF estimates both the T_b and a scaling factor for atmospheric water vapor C simultaneously. This joint estimation enables better correction of atmospheric effects on the fire signal anomaly and improves the accuracy of sub-pixel fire property retrievals. This is formulated in the Bayesian framework as follows:

$$p(T_b, C \mid L^{\text{obs}}(\boldsymbol{\lambda})) \propto p(L^{\text{obs}}(\boldsymbol{\lambda}) \mid T_b, C) \cdot p(T_b) \cdot p(C) \tag{4}$$

The forward model $L(T, \boldsymbol{\lambda})$, which maps physical parameters to observed radiance, is defined as:

$$L(T, \boldsymbol{\lambda}) = \frac{\int_0^\infty \tau(\boldsymbol{\lambda})\, \epsilon(\boldsymbol{\lambda})\, P(\boldsymbol{\lambda}, T)\, \Phi(\boldsymbol{\lambda})\, d\boldsymbol{\lambda}}{\int_0^\infty \Phi(\boldsymbol{\lambda})\, d\boldsymbol{\lambda}} \tag{5}$$

where, $P(\boldsymbol{\lambda}, T)$ is the Planck function at temperature T, $\epsilon(\boldsymbol{\lambda})$ is the surface emissivity, $\Phi(\boldsymbol{\lambda})$ is the sensor spectral response function, and $\tau(\boldsymbol{\lambda})$ is the atmospheric transmittance.

To isolate the effect of water vapor on transmittance, we factorize $\tau(\lambda)$ into a water vapor dependent term and a fixed background term:

$$\begin{aligned} \tau(\boldsymbol{\lambda}) &= \exp\left(-\frac{\sum_i m_i \alpha_i(\boldsymbol{\lambda})}{u}\right) \\ &= \exp\left(-\frac{m_{\text{bg}}\alpha_{\text{bg}}(\boldsymbol{\lambda}) + C \cdot m_{\text{wv}}\alpha_{\text{wv}}(\boldsymbol{\lambda})}{u}\right) \end{aligned} \tag{6}$$

where m_i are column densities of each trace gas, $\alpha_i(\lambda)$ are mass extinction coefficients of each trace gas, and u is the air mass factor, determined by the view zenith angle. The scaling factor C is introduced to estimate the total column water vapor content by scaling a wavelength independent reference profile. This approach reduces the dimensionality of the retrieval problem while preserving the spectral dependence of absorption through known mass extinction coefficients, improving estimation stability and interpret ability.

3.2.2. Fire Properties Estimation via Bayesian Framework

As illustrated in Fig. 1, fire property estimation in McBEF follows a decision tree structure. McBEF adopts the bi-phasic fire parametric model as its primary retrieval framework. Table 1 summaries the prior used by the McBEF implementation to VIIRS FILDA-2. As a first step, McBEF attempts the No-U-Turn Sampler (NUTS, Hoffman et al., 2014), an adaptive variant of the Hamiltonian Monte Carlo (HMC) approach, as the primary sampling strategy. The NUTS strategy dynamically tunes the trajectory length by adaptively determining the number of leapfrog steps, eliminating the need for manual tuning and making it particularly suitable for complex, high-dimensional models. However, it still relies on smooth gradient information to accurately simulate Hamiltonian dynamics. Observation noise, data anomalies, or truncated priors can introduce non-smoothness into the posterior distribution, leading to unstable gradients, leapfrog integrator failures, or violations of the *no U-turn* condition, thereby impairing sampling efficiency or convergence. In cases where NUTS fails due to gradient issues, McBEF falls back to the Metropolis algorithm. To mitigate the Metropolis sampler's sensitivity to initialization, we first compute a maximum–a–posteriori (MAP) estimate using the Limited–memory–Broyden–Fletcher–Goldfarb–Shanno Bounded (L–BFGS–B) optimization algorithm (Zhu et al., 1997). This MAP estimate serves as the starting point for Metropolis sampling. If the sampler still fails after reverting to Metropolis, McBEF further simplifies the fire model by downgrading from the bi-phasic assumption to a mono-phasic assumption, again attempting sampling sequentially via NUTS or Metropolis. This fallback is particularly important for cases dominated by heavy smoldering or residual burning, where no clear flaming component is present and the bi-phasic model becomes difficult to constrain.

Table 1: Priors for the Bayesian estimation

Phase	Temperature[1]	Fractional area
Flaming	$T_f \sim U(900, 1800)$	$\log\ p_f \sim U(-6, -0.3)$
Smoldering	$T_s \sim U(320, 900)$	$\log\ p_s \sim U(-6, -0.3)$
Mean	$\bar{T} \sim U(320, 1800)$	$\log\ \bar{p} \sim U(-6, -0.3)$
Background	$T_b \sim U(295, 25)$	

[1] Temperature range for different phase are adopted from Rein (2016) and Ward (2001).

4. Results

Evaluating McBEF's nighttime performance is particularly challenging due to the scarcity of *in situ* nocturnal fire measurements. Observational and safety constraints generally preclude the availability of ground-truth data during active nighttime burns. While some astellite-based high-resolution nighttime measurements (∼100 m) from the Advanced Spaceborne Thermal Emission and Reflection Radiometer (ASTER) and the Landsat series exist, they are typically subject to a 1–4 hour time lag relative to VIIRS overpasses. This delay is problematic for the validation of wildfire sub-pixel characterization, as fire conditions can evolve rapidly within such timeframe, rendering sub-pixel comparisons problematic.

Nonetheless, as demonstrated in the companion Part I, once radiative closure is achieved, the bi-phasic fire model provides physically meaningful estimates. These estimates may not always correspond to very tight uncertainties for temperatures and fractional areas, but they yield more reliable estimates of FRP, VEF, and heat flux, quantities with direct relevance to biomass burning characterization. As such, one important goal of this validation effort is to assess whether the retrieved parameters lead to radiative closure.

Moreover, while biomass burning temperatures often fluctuate over short timescales, anthropogenic combustion sources, such as gas flaring, exhibit relatively stable thermal behavior. This temporal stability relaxes the time-matching constraint, making them more suitable targets for validation using ASTER and Landsat observations. In addition, nighttime hyperspectral measurements from the Tropospheric Emissions: Monitoring of Pollution (TEMPO) mission provide another potential validation reference.

In this section, we first evaluate background temperature retrievals against the standard VIIRS land surface temperature (LST) product (VNP21). Next, we compare McBEF retrievals with ASTER and TEMPO data over gas flaring sites to demonstrate the quality and consistency of the fire parameter estimates. We also cross-validate results using near-simultaneous overpasses from the Suomi-NPP and NOAA-20 VIIRS instruments to assess retrieval consistency across platforms. A broader global assessment is provided in Section 4.3.

4.1. Evaluation of Background Temperature Estimation

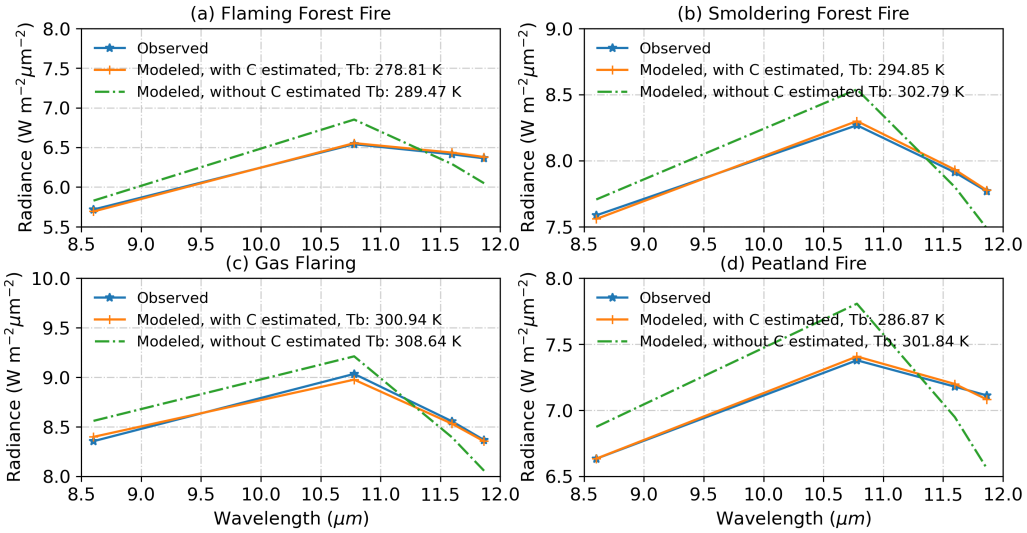

Figure 5: Comparison of the reconstructed background radiance with their ground truth for the selected cased in Fig.2.

Fig. 5 presents examples of reconstructed background radiance (orange line) for selected cases from Fig. 2. These reconstructions are based on McBEF-estimated background temperatures, jointly retrieved with a water vapor scaling factor. For comparison, we also show radiance reconstructed using background temperatures estimated without considering water vapor absorption (green line), along with the observed radiance (blue line). Surface emissivity is incorporated using the 8-day composite product VNP21A2. When atmospheric attenuation is ignored in the temperature estimation, the resulting reconstructed radiance overestimates spectral contrast between VIIRS bands M15 (10.5 μm) and M16 (12.01 μm), leading to a residual of

0.24 $Wm^{-2}sr^{-1}um^{-1}$. Incorporating the water vapor correction significantly reduces this discrepancy, yielding better spectral agreement with the observed radiance.

Fig. 6 provides a case study of the Williams Flats fire event on August 8, 2019. Background temperatures are estimated not only at the fire pixels (highlighted with red hatching) but also across surrounding clean-sky pixels using the same McBEF configuration (Fig. 6a). As shown, the resulting temperature field is spatially smooth. These McBEF estimates are compared against the operational VIIRS Land Surface Temperature (LST) product (Fig. 6b), showing highly consistent spatial patterns. The corresponding scatter plot (Fig. 6c) reveals a strong correlation ($R = 0.97$) and a root mean square error (RMSE) of 1.56 K. A slight warm bias is observed in the McBEF estimates relative to VIIRS LST, which likely stems from differences in emissivity treatment: McBEF uses an 8-day average emissivity product, which evolves with satellite overpass cycles but may be less representative of day-to-day surface changes. In contrast, the VIIRS LST algorithm estimates instantaneous emissivity dynamically, though its estimates may be influenced by near-surface water vapor and fire-emitted aerosols.

Rather than claiming one method is superior, this comparison demonstrates that McBEF's background temperature and water vapor scaling factor estimates are physically reasonable and closely align with the validated VIIRS LST product. Importantly, incorporating atmospheric correction using the estimated water vapor scaling factor enables physically meaningful radiative closure–not only for background estimation, but also as a critical prerequisite for retrieving fire temperature and other sub-pixel fire properties.

4.2. Evaluating retrieved fire temperature for gas flares

To demonstrate McBEF's sub-pixel fire characterization capability, we examine a gas flaring event in Texas on June 29, 2024. On this day, NOAA-20 VIIRS overpassed the region at 08:24 UTC with a satellite view zenith angle of 11°, and Landsat 8 captured a nighttime overpass at 04:39 UTC. Fig.7 shows the aerial imagery of the flaring site (panel a), VIIRS observations at 1.61μm and 2.25 μm (panels b and c), and Landsat 8 observations at 1.6 μm and 2.2 μm (panels d and e). The white boxes mark the VIIRS pixel footprints, and the red boxes show the higher-resolution Landsat footprints. Only one active flare source is apparent in the aerial imagery. This heat source causes a clear radiance enhancement in the VIIRS 1.61 and 2.25 μm bands. The Landsat data, with its higher spatial resolution, reveals more

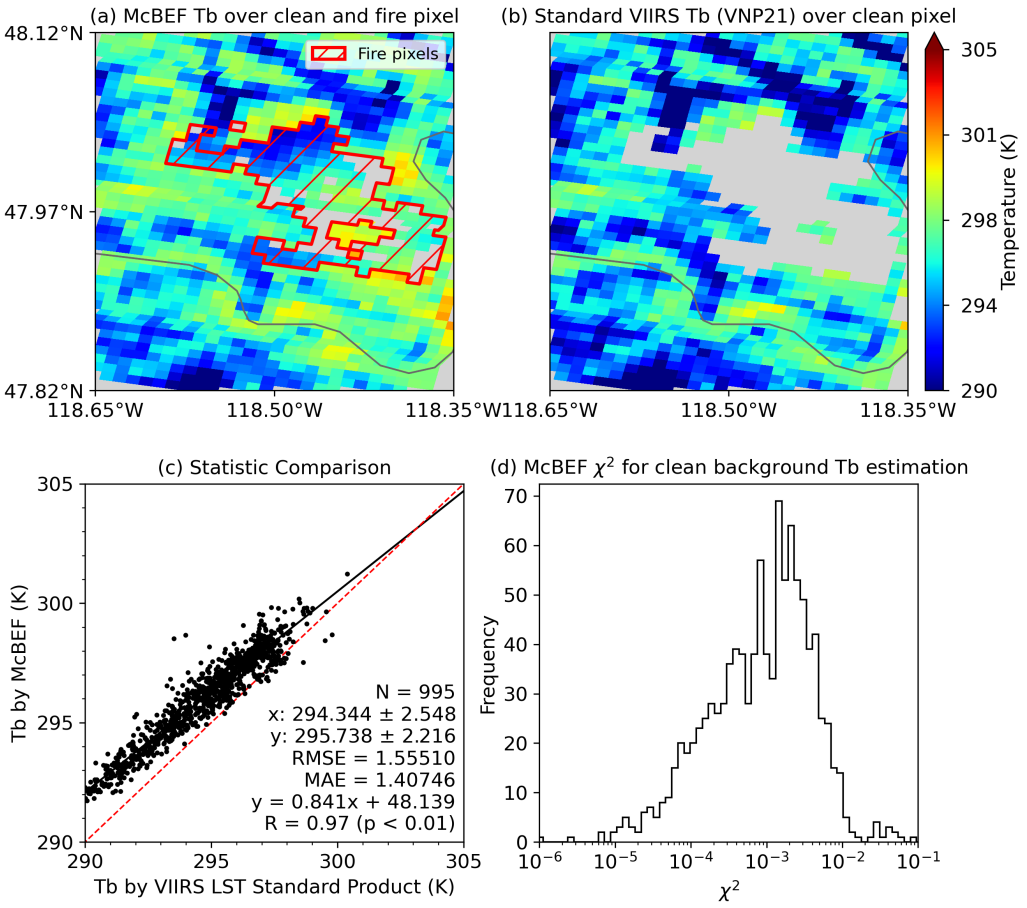

Figure 6: Case demonstration for background estimation.

intense anomalies near the flare site, especially in the two core pixels, each exceeding 50 $Wm^{-2}sr^{-1}um^{-1}$at 1.6μm.

Applying McBEF to the VIIRS FILDA-2 detections (VJ1 platform), we retrieved a flaming temperature of 1826–1895 K and a flaming area of 2.94–3.45 m^2 (Fig.8). Using a mono-phasic assumption (reasonable given the ∼30m Landsat resolution), a comparison with Landsat 8 yields a peak temperature of 1864 K and a total flaming area of 2.7 m^2. These results are consistent with the McBEF retrievals. Interestingly, McBEF also retrieved a smoldering component with a temperature of 440K to achieve radiative closure. Landsat, lacking MIR and TIR sensitivity, cannot independently validate this cooler component. Nonetheless, the estimated smoldering tem-

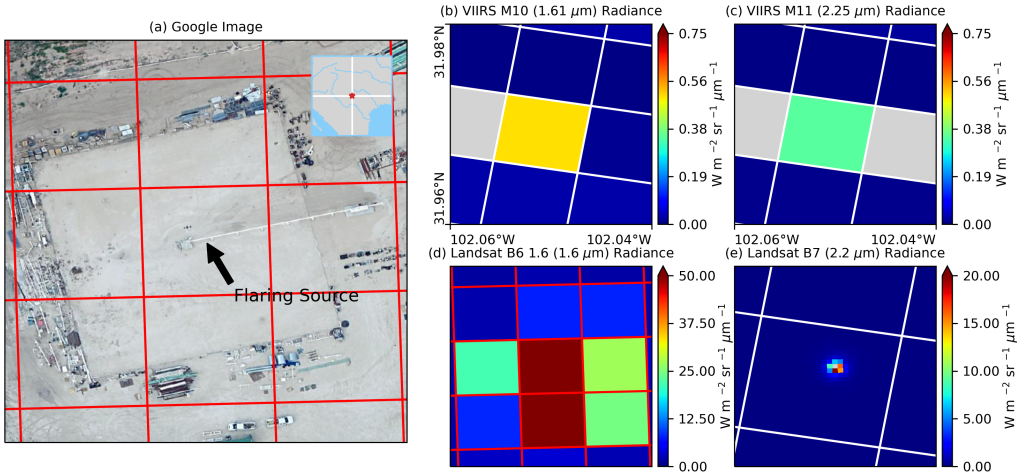

Figure 7: Google image and radiance measurements of the selected case. (a) Google aerial image of a gas flaring site over Texas. VIIRS observations at 1.6 μm for this site; (c) same as (b) but for VIIRS 2.25 μm. (d) and (e) are the Landsat observations in 1.6 μm and 2.2 μm. (d) and (e) are zoom in in different levels to provide a clear visualization. The red boxes on the (a) and (d) shows the LandSat footprint, in a spatial resolution of 30 meters. The white boxes on (b), (c), and (e) are the VIIRS footprints in a resolution of ∼800 m.

perature is physically plausible–it likely reflects heated infrastructure such as burner tips, flare stacks, and piping. Notably, the High Density Interval (HDI) of the retrieved flaming temperature is narrower than that of the smoldering component, indicating higher confidence in the flaming estimate. This also aligns with the reconstructed radiance profiles: radiance uncertainties are smaller in bands below 4 μm compared to those in MWIR and TIR as shown in Fig.8f.

For cross-sensor validation, we also applied McBEF to VIIRS observations from the Suomi NPP (VNP) overpass at 08:00 UTC, which occurred at a 45° view zenith angle. Fig A.17 shows the corresponding 1.64 and 2.2 μm radiance observed by the VNP. As expected, due to a larger view zenith angle, the VNP pixel size (1,024,314 m^2) is roughly 1.7 times larger than the near-nadir VJ1 pixel (586,815 m^2), resulting in a visibly weaker signal at bands that sensitive to the flaring, such as the 1.64 and 2.2 μm. However, the retrieved background temperatures agree closely: 301.82 K from VNP and 301.24 K from VJ1 with a 0.6 K difference. VNP also yielded a flaming

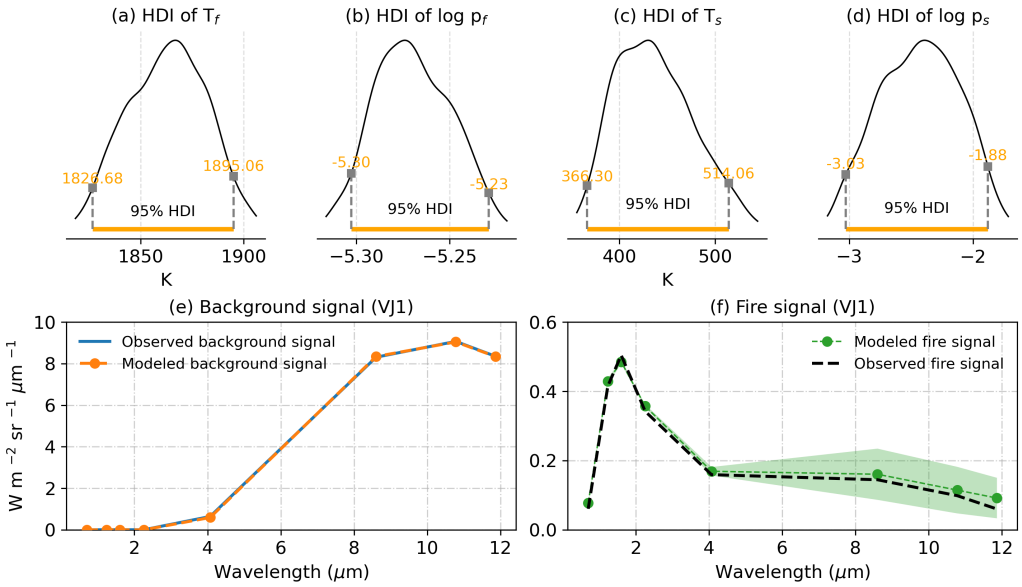

Figure 8: HDI of the estimated fire parameters and reconstruct radiance of the selected case based on VJ1 VIIRS observation.

temperature HDI of 1864–1935K, moderately consistent with the VJ1 and Landsat results. The retrieved flaming area was 3.39–3.98 m^2, which, assuming an ellipsoidal flame shape, can be corrected for viewing geometry based on the satellite zenith angle (Elvidge et al., 2015), yielding an adjusted area of 2.40–2.82 m^2, closely matching the estimates from VJ1 and Landsat.

As emphasized in the introduction, a comprehensive validation of fire temperature retrievals is inherently difficult due to sparse, time-limited ground truth data. This gas flaring case, though a single example, highlights McBEF's robustness across sensor platforms and view geometries. It underscores the algorithm's consistency and physical soundness in retrieving sub-pixel fire properties. However, it also illustrates the urgent need for higher-fidelity fire observations, spatially, temporally, and spectrally, to better support algorithm evaluation and development. Future work should focus on acquiring and leveraging such datasets, including but not limited to gas flaring, to advance validation efforts.

4.3. Global assessments of McBEF sub-pixel fire properties

The global assessment of the McBEF product focuses on three key aspects, reflecting the theoretical findings from Part I. First, we analyze the

partitioning of combustion phases—one of McBEF's main advancements–by examining the global distribution of combustion temperatures to characterize fire behavior across biomes. Second, the successful decomposition of fire phases enables direct calculation of fire FRP using the Stefan-Boltzmann Law. In Part I, we showed that the widely used empirical regression method by Wooster (the WS approach), based on 4 μm radiance, can introduce FRP uncertainties of up to 80%. In contrast, McBEF's physically based temperature estimates achieve radiative closure, reducing this uncertainty to about 3%. While this result is demonstrated in an OSSE framework, it remains important to assess its practical impact using real observations. Finally, we focus on the flaming combustion component, which drives vertical smoke injection into the atmosphere. We investigate whether McBEF's retrieved flaming temperatures can inform fire weather modeling, particularly in distinguishing extreme fire events that trigger pyrocumulonimbus (pyroCb) development from more typical boundary-layer fires.

4.3.1. Global distribution of fire temperatures

Fig. 9 depicts the global annual McBEF temperature distribution averaged to a 0.25 ° climate modeling grid. The radiative mean temperature is derived from the flaming and smoldering temperature and their corresponding fraction area via Stefan–Bolzmann Law, given by,

$$\bar{T} = \left(\frac{a_s T_s^4 + a_f T_f^4}{a_s + a_f} \right)^{\frac{1}{4}} \tag{7}$$

As shown in Fig. 9, flaming temperature displays a distinct spatial pattern that corresponds with International Geosphere-Biosphere Programme (IGBP) land surface types (Fig. 9d), reflecting the influence of fuel characteristics on wildfire combustion. Open-canopy ecosystems such as savannas, grasslands, and shrublands consistently exhibit higher mean flaming temperatures than forests. This contrast is especially pronounced when comparing the grassland-savanna belt of sub-Saharan Africa with the Amazon basin, dominated by evergreen broadleaf forests. Elevated flaming temperatures are also observed over cropland regions, notably in India and Eastern Europe.

Forested ecosystems often exhibit lower flaming temperatures, likely due to limited oxygen circulation resulting from dense canopy structure and high fuel compaction (Banerjee et al., 2020; Melnik et al., 2021). These factors

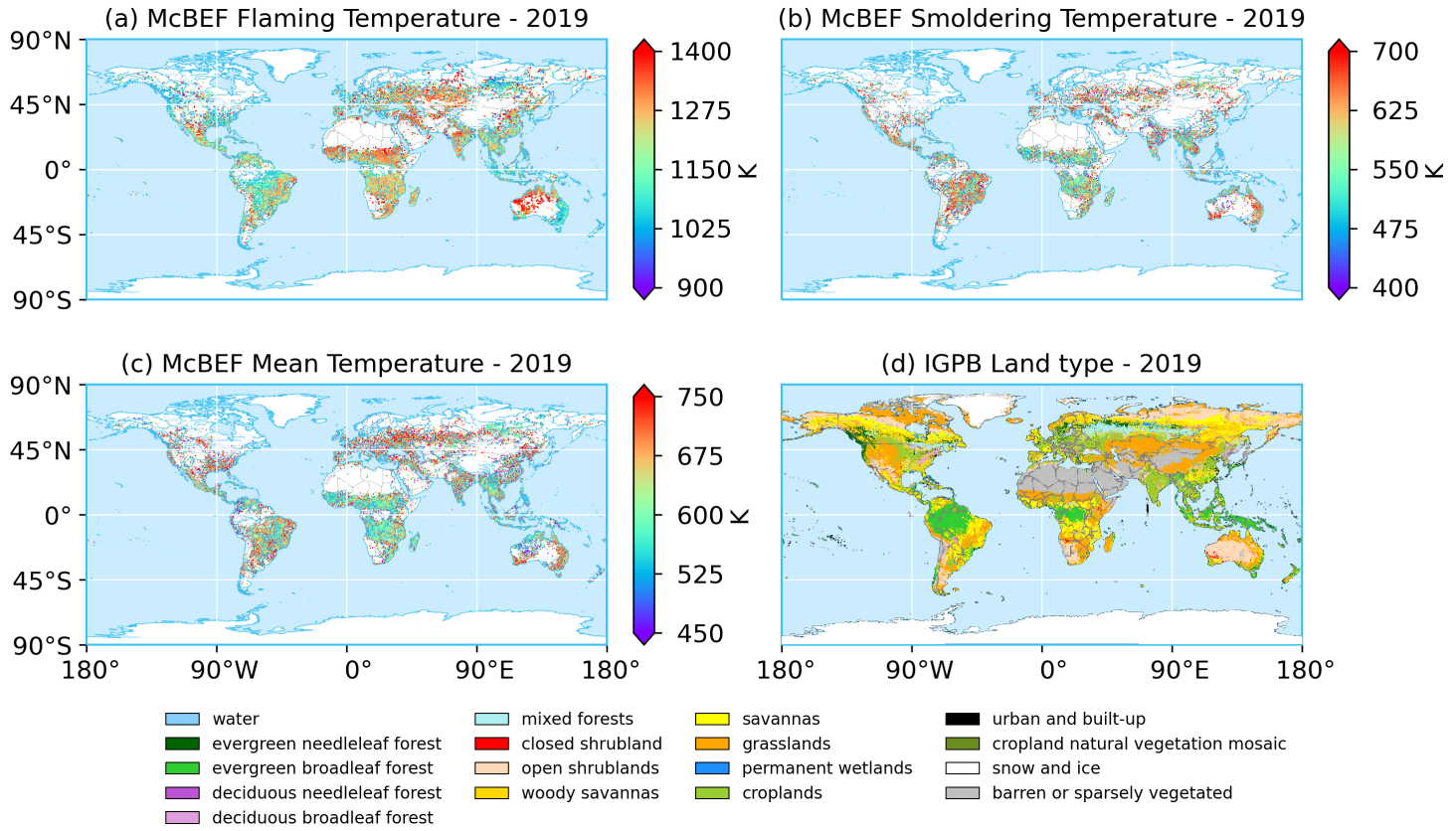

Figure 9: Global spatial distributions of the retrieved fire temperature. (a) Flaming temperature; (b) Smoldering temperature;(c) Mean temperature;(d) IGBP land surface type.

reduce combustion efficiency, thereby lowering flaming temperatures even during the active flaming phase. In contrast, grassland-like ecosystems, including croplands, are generally drier and more open, which promotes greater oxygen flow. These conditions support well-oxygenated, fast-moving flaming combustion, resulting in higher flame temperatures. Fuel moisture may also play a role, as the dense canopy structure of forest ecosystems tends to retain humidity, leading to higher moisture content in surface and understory fuels. A portion of the heat released during combustion must be used to evaporate this moisture (i.e., latent heat consumption), which in turn limits the energy available to raise the flame temperature. This effect may further suppress flaming temperatures in forested burns. It is also worth noting that in densely forested regions, canopy shading and geometric blocking may attenuate the observed fire radiance, further contributing to lower retrieved flaming temperatures.

In contrast, the spatial pattern of smoldering temperature appears reversed: grasslands tend to exhibit lower smoldering temperatures compared to forests. This suggests that in grassland-like ecosystems, the two combustion phases are more distinct–i.e., flaming and smoldering temperatures are more clearly separated–whereas in forests, combustion may be more thermally homogeneous. This likely reflects differences in post-flame fuel availability and combustion persistence. In grassland ecosystems, the rapid consumption of fine fuels during the flaming phase leaves little residual biomass to support extended smoldering, resulting in short-lived, low-temperature smoldering. In contrast, forest ecosystems typically contain dense and compacted fuel beds, such as duff, litter, and downed woody debris, that continue to burn slowly after the flaming front passes. These residual fuels sustain higher smoldering temperatures over longer durations, especially under the insulating conditions of dense canopy cover (Loudermilk et al., 2022). The canopy acts like a thermal lid, and the deep forest fuel bed functions as a heat reservoir. Together, they enable longer-lasting, hotter smoldering combustion than what is possible in open ecosystems like grasslands (Carmignani et al., 2024).

These systematic differences are also evident in the kernel density estimates (KDE) derived for each land surface type, as shown in Fig. 10. The flaming temperature peaks for forested ecosystems are generally below 1050 K, while those for grassland-like ecosystems peak above 1200 K. Some biome affinities are also reflected in the KDE curves–for example, deciduous broadleaf forests exhibit a similar flaming temperature distribution to that

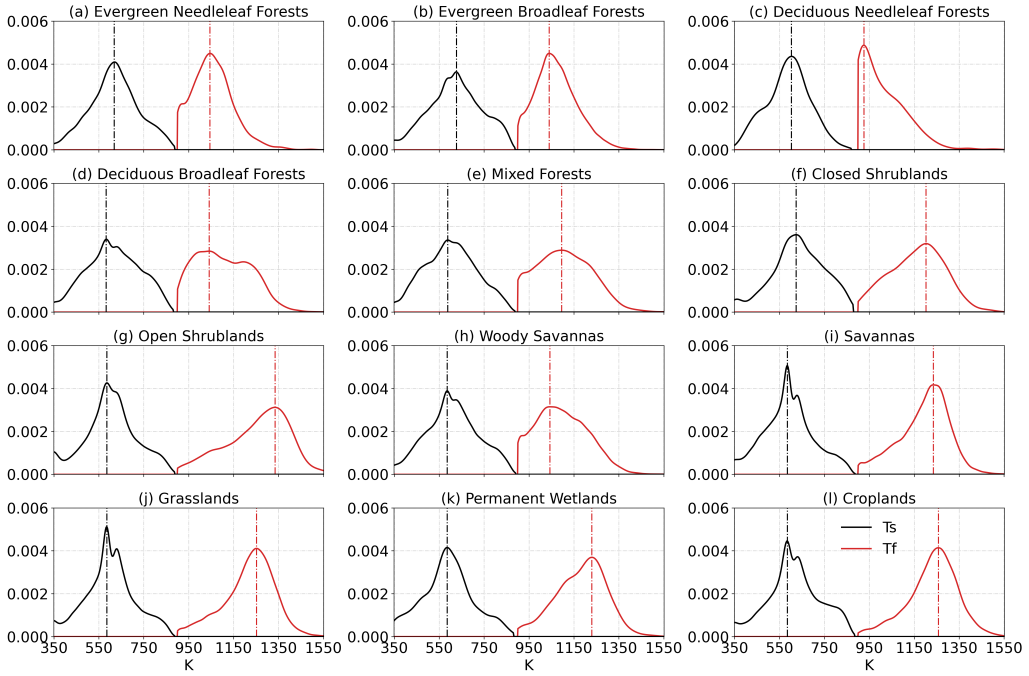

Figure 10: The kernel density estimation of the retrieved smoldering (black) and flaming (red) temperature over different land sruface type.

of mixed forests. This similarity likely stems from their ecological overlap, as temperate deciduous forests and mixed forests are often treated as a unified biome encompassing both hardwood-dominated stands and adjacent regions with mixed conifer-broadleaf composition (Gilliam, 2016). Fig.10 further reveals a consistent decline in peak flaming temperature with increasing shrub or tree cover. For instance, flaming temperature over shrublands peaks near 1150 K (Fig.10f), compared to a much higher peak of 1350 K in open shrublands (Fig.10a). Similarly, woody savannas exhibit lower peak flaming temperatures ($\sim$1050 K) than savannas ($\sim$ 1200 K). These patterns emphasize that oxygen availability is a primary driver of flaming temperature during the active combustion phase. It is also worth noting that in 2019, less than 3,000 fire detections were recorded over deciduous needleleaf forests–substantially fewer than those for other land cover types. As a result, the KDE curve for this class is less statistically robust and should be interpreted with caution.

Fig.11 further investigates the seasonality of flaming temperatures across Australia and New Zealand. This region is chosen because of its persistent

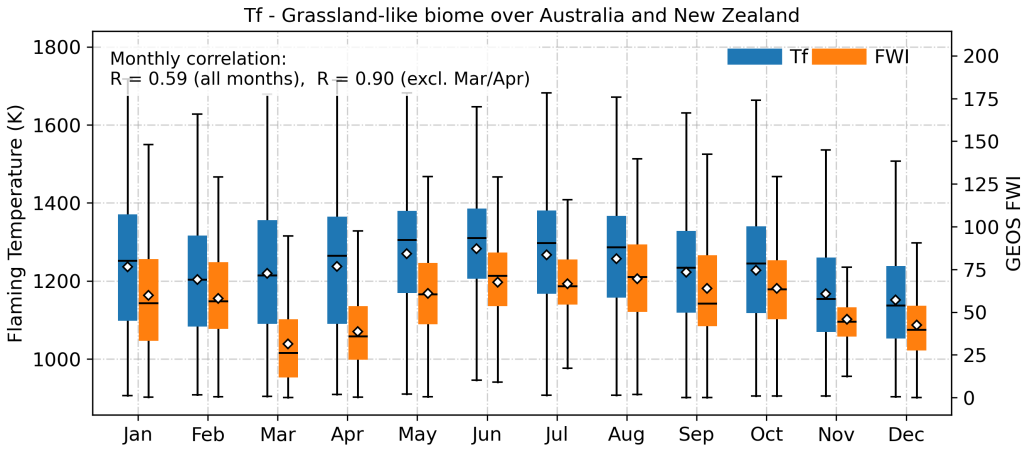

Figure 11: Seasonal cycle of the flaming temperature and GEOS fire weather index for the grassland-like boime over Australia and New Zealand.

wildfire activity, predominantly over grassland-type bioma throughout the year, providing sufficient data for a robust seasonal analysis. By contrast, seasonal signals are less apparent in regions such as North America, Amazon, or Africa, due to greater biome diversity and limited fire activity in certain months, as illustrated in Fig. A.19.

As shown, the monthly flaming temperature exhibits a clear seasonal cycle aligned closely with the well-documented regional fire season. Specifically, flaming temperatures gradually increase from May, peak between July and August, and then progressively decline through December, before rising again slightly in January and February. This pattern closely corresponds with the Fire Weather Index (FWI, Alexander and Groot, 1988) available in Global Fire WEather Database (GFWED). The FWI is a widely adopted metric summarizing wildfire intensity potential based on local meteorological conditions, including fuel moisture, drought severity, precipitation, temperature, relative humidity, and wind. During July and August, when the FWI reaches its annual peak, the flaming temperatures are also systematically higher. Subsequently, as the FWI decreases from September through December, flaming temperatures follow suit. However, this alignment weakens for March and April, although the general trend—higher FWI in April compared to March—is still reflected in flaming temperatures. This discrepancy likely results from the significantly reduced number of detectable fires in these months; for example, fire detections drop below 3,000 during March

and April, compared to approximately 6,000 in June and July and several thousand in November and December.

Overall, the monthly correlation between FWI and flaming temperature is 0.59; however, excluding the sparse data from March and April increases this correlation to approximately 0.9. This strong alignment underscores the relatively homogeneous biome composition and consistent climate patterns within the Australian region. In contrast, regions such as southern hemisphere Africa (Fig.A.19) show less distinct seasonal cycles, primarily due to their complex biome mixtures and varied climatic patterns. However, restricting analysis solely to fire events south of the Tropic of Capricorn reveals a more defined seasonal cycle (Fig.A.20), where the correlation between FWI and flaming temperature improves significantly to 0.7.

4.3.2. Evaluation of Fire Radiative Power (FRP)

FRP density, defined as the FRP divided the pixel area, is the fundamental quantity informing top-down biomass burning emission estimates (*e.g. Darmenov and da Silva, 2015)*. There are three main sources of uncertainty affecting the estimation of FRP densities: atmospheric absorption, sensor detection limitations, and the intrinsic limitations of the classic Wooster empirical regression method based on 4 μm radiance (hereafter the WS approach). Atmospheric absorption, primarily due to water vapor and other trace gases, results in a sinusoidal angular dependence of FRP estimates, as previously demonstrated by Deng et al. (2024). At nadir, the shorter atmospheric path length reduces attenuation of fire radiance, leading to higher FRP densities, while at the end-of-swath (EOS), longer path lengths increase attenuation and thus decrease FRP densities. Sensor detection limitations, arising from the minimal detectable radiance threshold, lead to small fires at EOS being frequently missed by detection algorithms. When calculating the mean FRP across the satellite swath, these small, undetected fires at the EOS naturally fall out of averaging, partially offsetting the expected attenuation-driven decline and contributing to a subtle angular dependence. Finally, the WS approach does not explicitly incorporate angular dependence but introduces significant uncertainties, particularly for smoldering-dominated fire events, as discussed extensively in Part I.

Fig.12a illustrates the angular dependence of FRP density derived from FILDA-2 and McBEF datasets, both with and without atmospheric correction (AC). The blue line shows FRP density derived from the WS approach using TOA 4 μm radiance (Wooster-Raw). The red line indicates FRP den-

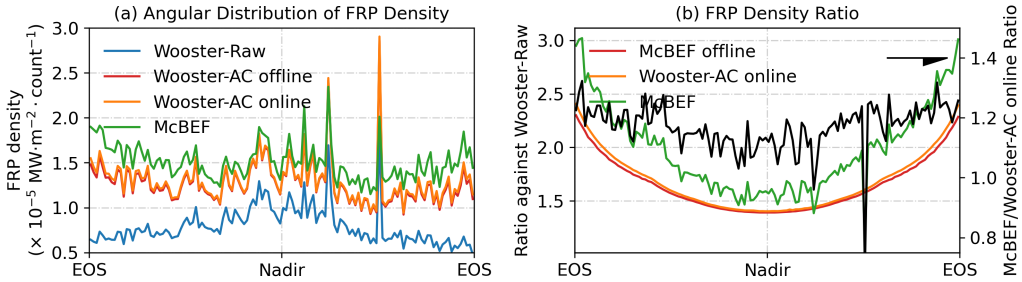

Figure 12: Angular distribution of the FRP density estimated from the nighttime fire detected by FILDA-2.

sity after applying offline atmospheric correction using GEOS-FP instantaneous total column precipitable water (Wooster-AC offline). Because McBEF estimates water vapor scaling factors individually for each detection, an online AC can be performed directly; the result is shown by the orange line (Wooster-AC online). Finally, the green line represents FRP estimates from McBEF based on retrieved temperatures using the Stefan-Boltzmann Law. Fig.12b shows the relative adjustments made for Wooster-AC (offline and online) and McBEF compared to Wooster-Raw, indicated by red, orange, and green curves, respectively. The black curve illustrates the ratio of McBEF to Wooster-AC online.

As depicted by the Wooster-Raw (blue line) in Fig. 12a, atmospheric absorption is the primary driver of angular dependence, resulting in a pronounced peak near nadir that diminishes toward the end of the swath (EOS). When atmospheric correction is applied, as shown by both Wooster-AC offline and online lines, this angular dependence is significantly reduced. The online AC, informed by observation-specific water vapor estimates from McBEF, offers a more accurate correction, particularly toward EOS, compared to the coarser-resolution model-based offline AC. Notably, McBEF-derived FRP density (green line) surpasses both Wooster-AC offline and online estimates, primarily because the radiative closure achieved through temperature retrieval reduces systematic biases inherent to the empirical regression method. Additionally, McBEF FRP density shows an upward trend toward EOS. This trend, also apparent in the black ratio line comparing McBEF to Wooster-AC online (Fig. 12b), aligns with expectations given the sensor's detection limitations that disproportionately remove smaller fire detections toward EOS in conventional methods.

Addressing the angular dependence in FRP density estimation signifi-

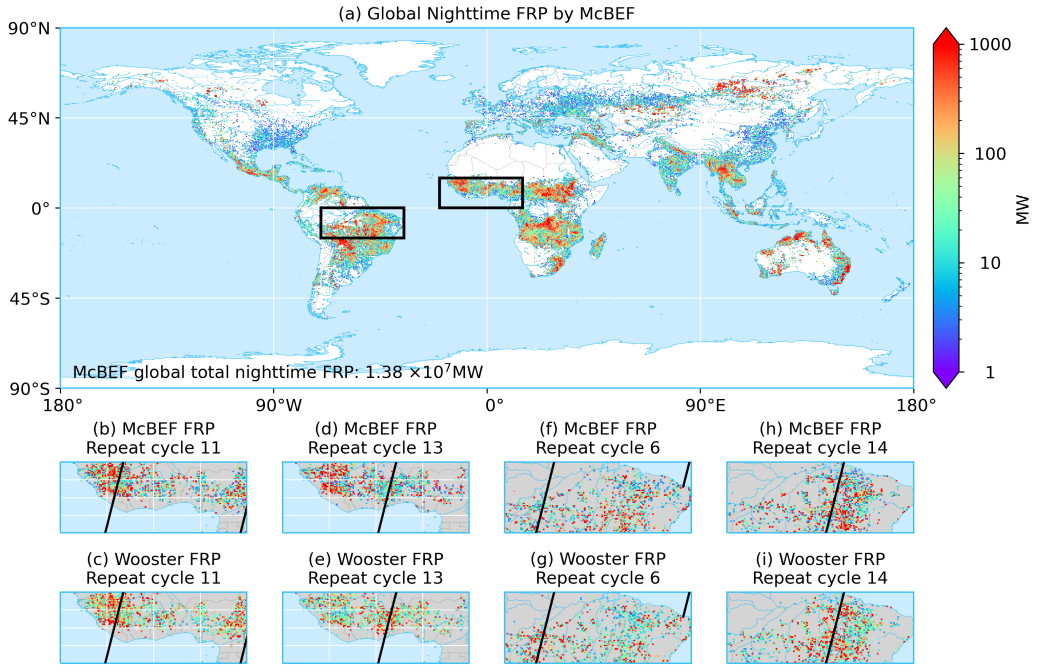

Figure 13: Angular distribution of the FRP density estimated from the nighttime fire detected by FILDA-2. The black boxes on (a) show the selected region to illustrate the FRP angular dependence. The black on lines on (b) to (i) indicate the position of the satellite nadir for each of the repeat cycle.

cantly influences fire emissions. Fig. 13a presents the global nighttime FRP distribution for 2019 derived from McBEF. Annually, the total nighttime FRP estimated by McBEF is 2.275×10^7 MW, comparable to previous studies (Deng et al., 2024). Excluding contributions from gas flaring and other anthropogenic sources, biomass-burning alone contributes 1.37×10^7 MW, an 84% increase over the 7.42×10^6 MW estimated using the WS approach. This substantial correction significantly reduces reliance on empirical scaling factors typically needed for top-down fire emission inventories such as QFED.

Angular dependence also introduces persistent temporal biases. For polar-orbiting satellites such as those in the JPSS constellation, which revisit the same location every 16 days, angular dependence creates a repeating pattern in FRP estimates that propagates into downstream emission inventories. This is particularly notable during periods reliant on single-satellite observations, such as 2012–2017 with S-NPP VIIRS alone. To illustrate this,

Figs. 13b–i compare mean FRP distributions across multiple repeat cycles over Northern Africa and the Amazon. The Wooster-Raw product exhibits clear inconsistencies, such as higher FRP values at nadir (repeat cycle 11) compared to lower values at EOS (repeat cycle 13). In contrast, McBEF-derived FRP shows a spatially consistent pattern across repeat cycles.

In constructing top-down fire emission inventories, while total biases in FRP estimates can sometimes be corrected empirically, angular biases and associated repeat-cycle inconsistencies are more challenging to address. McBEF's physically consistent, radiatively closed FRP estimates provide a valuable alternative for robust, accurate input into fire emission inventories.

4.3.3. Implications for Plume Rise Modeling

Beyond improving FRP estimation, a key advantage of McBEF is its ability to partition fire temperatures, yielding phase-specific inputs for emission coefficients and plume-rise. Plume-rise models (PRMs), such as the Freitas scheme (Freitas et al., 2007), are driven by the *flaming-phase sensible (convective) heat flux*. In many modeling studies, that flux is approximated as proportional to the radiative heat flux, which itself is inferred by empirically scaling bulk FRP density; for example, Val Martin et al. (2012) explored several alternatives to estimate sensible heat flux from FRP. However, regardless of the specific formulation used in these scaling approaches, the underlying assumption is effectively equivalent to prescribing a fixed fire-affected fraction within the model grid. This assumption enables the conversion of FRP, expressed in watts (W), into radiative heat flux in units of $\mathrm{W} \cdot \mathrm{m}^{-2}$. While convenient, this shortcut introduces three major sources of uncertainty.

First, radiative heat flux depends primarily on the burning temperature via the Stefan-Boltzmann law ($Q_{\mathrm{rad}} \propto T^4$), whereas sensible heat flux depends on multiple factors, most importantly the temperature contrast between the flame and ambient air and the efficiency of turbulent heat transfer (e.g., $Q_{\mathrm{conv}} \propto H(T_f - T_b)$, with H influenced by wind speed, roughness, and stability). Second, although FRP density has units of $\mathrm{W} \cdot \mathrm{m}^{-2}$, it is computed by normalizing total FRP by the *entire* pixel area, typically far larger than the burning fraction. This geometric dilution biases radiative flux low in a way that a global scale factor cannot correct. Third, FRP integrates radiative power from *all* combustion phases and cannot resolve sub-pixel heterogeneity or separate flaming from smoldering; only the flaming component is generally capable of lofting smoke above the boundary layer, while smoldering emissions tend to remain within it. Consequently, estimates based

solely on bulk FRP density do not faithfully represent the flaming-phase sensible heat flux that sets plume buoyancy. Peterson et al. (2014) showed that even sub-pixel, mono-phasic temperature retrievals improve plume-rise predictions. McBEF goes further by retrieving phase-specific temperatures and fractional areas, enabling a physically grounded estimate of the *flaming* sensible heat flux and more accurate coupling to 1-D PRMs and fire-atmosphere models—particularly during extreme events when radiative and sensible fluxes can decouple.

As an illustration, we compare the flaming sensible/convective heat flux (Fig. 14) and the radiative heat flux (Supplement, Fig. A.21) retrieved by McBEF for pyroCb events against the global 2019 distribution. PyroCb cases were identified using the published event database of Fromm et al. (2022) and Peterson et al. (2025). For each event, we extract associated fire clusters within a 20 km radius of the event center and select the top ten flaming-phase temperature retrievals per cluster. We use the bulk formulation of convective heat flux (Liu et al., 1979; Freitas et al., 2007)

$$Q_{\text{conv}} = \rho c_p C_H U (T_f - T_b) \tag{8}$$

to calculate the convective heat flux; where $\rho \approx 1.2\ kg \cdot m^{-3}$ is air density, $c_p \approx 1005\ J \cdot kg^{-1} \cdot K^{-3}$ is air density, C_H is turbulent (bulk) heat transfer coefficient, and U is characteristic wind speed at the interface sampled from the GEOS forward-processing, time-averaged land-surface forcing dataset and temporally interpolated to the observation time.

More than 60% of the sampled pyroCb events occurred in evergreen forest and ∼30% in woody savanna. As shown in Fig. 14 and Fig. A.21, pyroCb events exhibit systematically higher flaming heat fluxes (red line)–both sensible and radiative–than the global distribution (black line). This elevated energy release suggests stronger buoyant forcing and thus a greater potential for high-altitude smoke injection. Such intense heat fluxes are characteristic of large, fast-spreading crown fires in dense fuels (e.g., evergreen forests), where rapid combustion drives deep convective columns. This is consistent with the known dynamics of pyroCb formation, which typically requires sustained flaming intensity and strong surface-atmosphere coupling to generate the vertical momentum needed to breach the lower troposphere and initiate cloud development.

Heat fluxes derived from mean temperatures (green and orange lines) are also significantly lower than those derived from flaming temperatures,

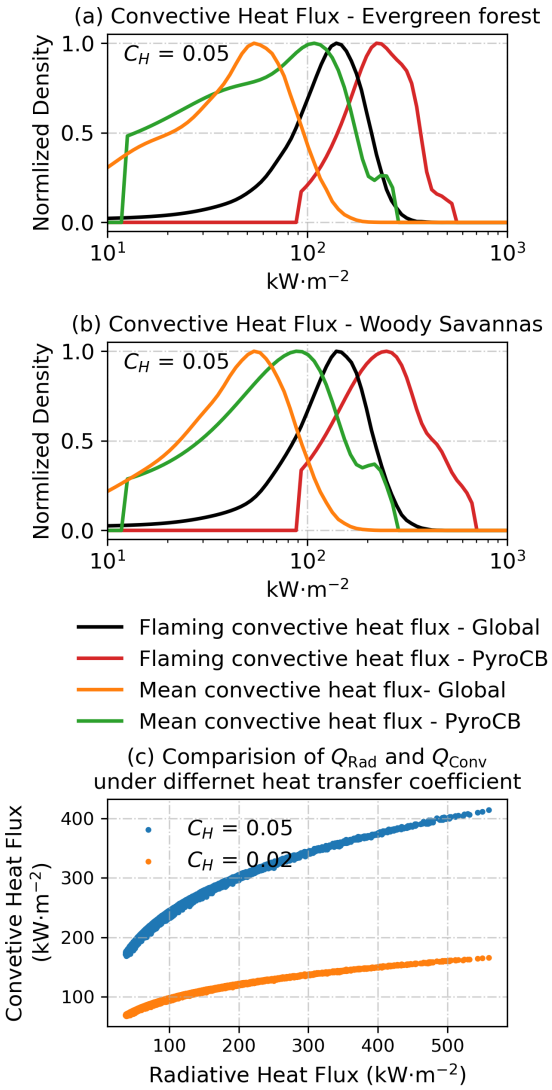

Figure 14: Kernel density estimation for the convective heat flux for the global and PyroCB events over (a) evergreen forest and (b) woody savannas using turbulent (bulk) heat transfer coefficient C_H=0.05. (c) is the comparison of the radiative heat flux and convective heat flux derived under C_H=0.02 (blue) and C_H=0.05 (orange) over evergreen forest. Black line is the flaming heat flux based on global fire events. Red line is the flaming heat flux over PyroCB events. Orange line is the mean heat flux based on global fire events. Green line is the mean heat flux over PyroCB events.

highlighting a key limitation of using mean temperature to estimate convective heat flux. As shown in Eq. 7, the mean temperature is calculated as a radiance-weighted average over both smoldering and flaming components. For most fires, the smoldering fraction is substantially larger than the flaming fraction, especially since flaming is typically confined to the narrow fire front. As a result, the mean temperature is biased toward the lower smoldering temperature, which leads to a systematic underestimation of the buoyancy-relevant heat flux. This aligns with findings from Freitas et al. (2007), who emphasized that vertical injection models (e.g., PRM) are most sensitive to the temperature of the buoyancy-driving flame front rather than the average fire temperature across the pixel. Therefore, mean temperature is not an ideal proxy for estimating the convective heat flux that governs plume rise.

However, because sensible flux reflects coupling to the ambient environment, its magnitude varies with turbulent exchange. We illustrate this sensitivity with two representative transfer coefficients. For moderate turbulent coupling $C_H = 0.05$, pyroCb events over evergreen forest yield Q_{conv} ~90–600 $kW \cdot m^{-2}$, slightly larger than or comparable to the corresponding radiative flux (~90–600 $kW \cdot m^{-2}$). Under weak coupling ($C_H = 0.02$), Q_{conv} over the same biome drops to ~25–200 $kW \cdot m^{-2}$). Figure 14c makes this point directly: for a fixed radiative flux (i.e., fixed flaming temperature), variations in C_H alone can change the sensible flux by a factor of 2-3.

These results highlight two implications. First, beyond the well-known geometric dilution in FRP density, even the radiative flux itself is an imperfect proxy for the flaming sensible flux that sets buoyancy in plume-rise models. Second, partitioning phase-specific temperatures and areas (as in McBEF) is a critical first step; equally important for reliable PRM coupling are credible environmental exchange parameters at the fire-air interface (e.g., C_H, U).

5. Discussion and Concluding Remarks

This study presents the application and evaluation of the Monte Carlo Biphasic Estimation of Fire Properties (McBEF) algorithm to nighttime VIIRS observations. Building on the theoretical foundation established in Part I, we demonstrate that McBEF is capable of robustly retrieving phase-specific fire temperatures and fractional areas from multi-spectral satellite data, underpinned by physically consistent background estimates. Our case

studies—including comparisons with Landsat 8 and multi-angle VIIRS overpasses—highlight McBEF's ability to provide stable retrievals across varying sensor configurations and viewing geometries.

At the global scale, McBEF reveals systematic spatial and seasonal patterns in flaming and smoldering temperatures that correspond closely with land cover and fire regimes. Importantly, the angular dependence observed in Fire Radiative Power (FRP) estimates from traditional approaches—largely driven by atmospheric attenuation and sensor detection limitations—is substantially reduced with McBEF. This improvement stems from the algorithm's physical radiative closure and enhances the reliability of FRP for use in fire emission inventories and downstream modeling applications.

Despite these advances, several limitations remain. Validation opportunities at night are constrained by the scarcity of coincident, high-resolution field measurements for wildfires, especially at night. While our targeted validation at gas flaring sites demonstrates McBEF's skill in retrieving physically consistent fire properties, more field observations–particularly over active wildfires–are needed to fully evaluate retrieval accuracy across diverse environments and fire behaviors.

It is also important to note that the current implementation of McBEF is optimized for nighttime fire observations, when solar illumination is absent and the challenges from reflected sunlight are minimized. Expanding the algorithm to daytime conditions will require addressing additional sources of uncertainty, such as solar contamination, increased background variability, and the need for more complex atmospheric corrections. Such developments will further broaden the operational applicability of McBEF and enable more comprehensive, around-the-clock fire monitoring. The night time results provide the first step toward day long estimates of fire properties.

Some structural limitations also remain inherent to the framework. McBEF does not explicitly account for canopy shading or geometric blocking in dense forest environments, where active flames may be obscured beneath the canopy. This leads to systematic underestimation of flaming temperature and fire area fraction, emphasizing the need for future retrieval algorithms to consider sub-canopy combustion and complex observation geometries. Additionally, although water vapor is treated as the primary source of atmospheric transmittance variability, emissions of trace gases from combustion (such as CO_2, N_2O, and CH_4) can further attenuate radiance in affected spectral channels, particularly during intense fire events. Future work will investigate the use of model-simulated smoke and trace gas fields to achieve

more comprehensive atmospheric correction.

McBEF's phase-specific partitioning supplies the physically relevant flaming sensible (convective) heat flux required by plume-rise models, avoiding the pitfalls of inferring buoyancy from radiative proxies (e.g., FRP density) that suffer geometric dilution and different physics (T^4 dependence vs. environmental coupling). Our pyroCb analysis shows systematically higher flaming fluxes than the global distribution, and demonstrates that sensible flux varies by factors of $\sim$2–3 with plausible changes in turbulent exchange (e.g., C_H) and near-surface wind U, whereas mean-temperature–based estimates understate buoyant forcing. Thus, partitioning is the essential first step, and credible environmental parameters at the fire–air interface are equally necessary for accurate plume-rise prediction and smoke-injection height.

Another strength of McBEF is the provision of full posterior distributions for all retrieved fire properties, which enables rigorous uncertainty quantification. Such probabilistic outputs can be directly leveraged in emissions inventories, risk assessment, and downstream atmospheric modeling, adding value over conventional deterministic approaches. While this study focused on nighttime VIIRS observations, McBEF is sensor-agnostic and has been demonstrated for other multi-spectral platforms such as SLSTR, positioning it for broader use as new sensors become available and as satellite capabilities evolve.

Ultimately, fully realizing the potential of sub-pixel fire characterization will require not only continued advances in retrieval algorithms, but also improvements in satellite sensor design, including higher spatial resolution, expanded spectral coverage, and enhanced radiometric sensitivity. Targeted field campaigns to collect coincident high-resolution measurements will also be crucial for ongoing validation. Together, these developments will enable more reliable and comprehensive fire retrievals, advancing both the science and operational management of wildland fire in a changing climate.

6. Data available statement

The VIIRS FILDA-2 L2 data is downloaded from Level-1 and Atmosphere Archive & Distribution System (LAADS) Distributed Active Archive Center (DAAC) (https://ladsweb.modaps.eosdis.nasa.gov/). The NASA GOES FWI is extraced from NASA Global Fire WEather Database (GFWED) (https://data.giss.nasa.gov/impacts/gfwed/). The Landsat obsevation is retrieved from the U.S. Geological Survey (USGS)

EarthExplorer website (https://earthexplorer.usgs.gov/). The VIIRS sensor response function are obtained from NOAA's Center for Satellite Applications and Research. (https://ncc.nesdis.noaa.gov/VIIRS/VIIRSSpectralResponseFunctions.php). The McBEF software is available at Goddard Earth Observing System-Earth System Modeling (https://github.com/GEOS-ESM/FILDA/tree/main/src/MCBEF).

7. CRediT authorship contribution statement

Meng Zhou: Writing - review&editing, Writing-original draft, Visualization, Validation, Software, Resources, Project administration, Methodology, Investigation, Formal analysis, Data curation, Conceptualization. Arlindo M. da Silva:Writing-review&editing, Methodology, Investigation, Formal analysis, Conceptualization, Funding acquisition. Jun Wang: Writing-review&editing, Software, Resources, Funding acquisition. David A. Peterson: Writing - review&editing, Formal analysis, Resources.

8. Acknowledgment

This work has been supported by NASA's MAP and MEaSURES programs. The authors acknowledge the Level-1 and Atmosphere Archive & Distribution System (LAADS) Distributed Active Archive Center (DAAC), located in the Goddard Space Flight Center in Greenbelt, Maryland, from where the VIIRS FILDA-2 and active fire data were retrieved. The authors thank NOAA's Center for Satellite Applications and Research (NOAA STAR) for maintenance of VIIRS sensor response function. The authors thank René Servranckx and Mike Fromm (NRL) for providing the access to the global pyrocumulonimbus dataset. The authors acknowledge Amber Soja and Emily Gargulinski at NASA Langley Research Center (LaRC) for discussion of the global temperature distribution. Special thanks are expressed to Gonzalo Ferrada (CIRES/NOAA) for the insight discussion across different stages of the McBEF development. As a response to the changing climate of open-source development, we gratefully acknowledge the PyMC developers and community for the PyMC probabilistic-programming framework, which we used for MCMC sampling (NUTS and Metropolis) in McBEF (Salvatier et al., 2016; Abril-Pla et al., 2023).

Appendix A. Supplementary materials

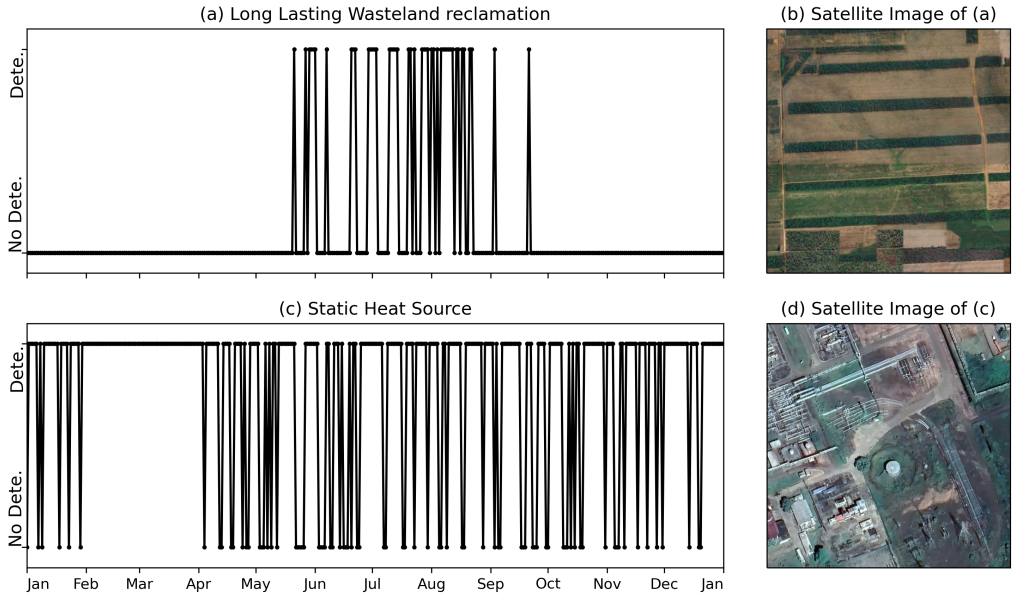

Figure A.15: Example of the frequency analysis for generating the static heat source using the VIIRS fire detection proudct. (a) and (b) 16-days fire detection time series and google image for a long lasting wasteland reclamation activity over South America; (c) and (d) 16-days fire detection time series and google image for a Industry heating over South America.

Table A.2: Variables in McBEF sampling dataset. A dash (—) indicates a unitless quantity. Dimensions use $N_{\text{fire}} = 8$ and $N_{\text{sample}} = 2000$. Variables with the `sample` dimension are MCMC draw arrays; others are per-fire scalars.

Variable	Dimensions	Long name	Units
FP_Time	(N_{fire})	Time since 2000-01-01 00:00:00 UTC	minutes
t_b	(N_{fire})	Background Temperature	K
C	(N_{fire})	Water Vapor Scaling Factor	—
QA_flag	(N_{fire})	Quality flag	—
FP_Power_R_AC	(N_{fire})	Radiance based FRP estimation with atmospheric correction	MW
t_s	(N_{fire}, N_{sample})	Smoldering Temperature	K
p_s	(N_{fire}, N_{sample})	Smoldering Fraction	—
t_f	(N_{fire}, N_{sample})	Flaming Temperature	K
p_f	(N_{fire}, N_{sample})	Flaming Fraction	—
FP_confidence	(N_{fire})	FILDA detection confidence	—
FP_Land_Type	(N_{fire})	MODIS Land cover product MCD12C1	—
FP_Gas_Flaring	(N_{fire})	Gas Flaring flag	—
Static_flag	(N_{fire})	Static source flag	—
FP_Peatland	(N_{fire})	Peatland flag	—
FP_Peatfrac	(N_{fire})	Peatland fraction	—
FP_SAA_flag	(N_{fire})	South Atlantic Anomaly	—
FP_Latitude	(N_{fire})	Latitude of fire pixel	degrees_north
FP_Longitude	(N_{fire})	Longitude of fire pixel	degrees_east
FP_Area	(N_{fire})	Pixel area	m^2
FP_Line	(N_{fire})	Granule line of fire pixel	—
FP_Sample	(N_{fire})	Granule sample of fire pixel	—
FP_VE	(N_{fire})	Visible light power	MW
FP_VEF	(N_{fire})	Visible Energy Fraction (VEF)	—
FP_MCE	(N_{fire})	Modified Combustion Efficiency (MCE)	—
FP_Power_R	(N_{fire})	Radiance based FRP estimation	MW
overpass	(N_{fire})	Index of the overpass time by every 6 minutes	—

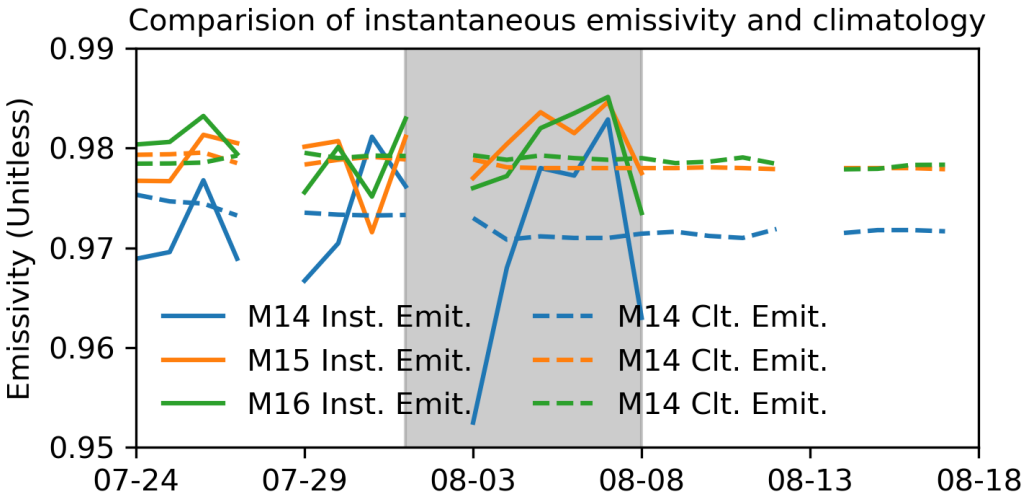

Figure A.16: Time series comparision of the instaneous emissivity and its climatology based on the VNP21A2 proudct.

Table A.3: Variables in McBEF statistic dataset. A dash (—) indicates a unitless quantity. Dimensions use N_f and N_s to represent the number of fire and the number of statistic summaries used. Where present, the `s` axis encodes summary statistics of the MCMC draws as: 0 = lower HDI bound, 1 = mode, 2 = upper HDI bound, 3 = mean, 4 = standard deviation.

Variable	Dimensions	Long name	Units
FP_Latitude	(N_f)	Latitude of fire pixel	degrees_north
FP_Longitude	(N_f)	Longitude of fire pixel	degrees_east
FP_Time	(N_f)	Time since 2000-01-01	minutes
t_b	(N_f)	Background Temperature	K
C	(N_f)	Water Vapor Scaling Factor	—
QA_flag	(N_f)	Quality flag	—
FP_Power_R_AC	(N_f)	Atmospheric corrected FRP	MW
FP_confidence	(N_f)	FILDA detection confidence	—
FP_Land_Type	(N_f)	IGBP Land cover product	—
FP_Gas_Flaring	(N_f)	Gas Flaring flag	—
Static_flag	(N_f)	Static source flag	—
FP_Peatland	(N_f)	Peatland flag	—
FP_Peatfrac	(N_f)	Peatland fraction	—
FP_SAA_flag	(N_f)	South Atlantic Anomaly	—
FP_Area	(N_f)	Pixel area	m^2
FP_Line	(N_f)	Granule line of f pixel	—
FP_Sample	(N_f)	Granule sample of f pixel	—
FP_VE	(N_f)	Visible light power	MW
FP_VEF	(N_f)	Visible Energy Fraction	—
FP_MCE	(N_f)	Modified Combustion Efficiency	—
FP_Power_R	(N_f)	Radiance based FRP estimation	MW
HeatFlux_s	(N_f, N_s)	Smoldering heat flux	MW m^{-2}
HeatFlux_f	(N_f, N_s)	Flaming heat flux	MW m^{-2}
Power	(N_f, N_s)	Fire radiative power	MW
Power_s	(N_f, N_s)	Smoldering fire radiative power	MW
Power_f	(N_f, N_s)	Flaming fire radiative power	MW
t_f	(N_f, N_s)	Flaming temperature	K
t_s	(N_f, N_s)	Smoldering temperature	K
p_s	(N_f, N_s)	Fractional smoldering area	—
p_f	(N_f, N_s)	Fractional flaming area	—
Area_s	(N_f, N_s)	Smoldering area	m^2
Area_f	(N_f, N_s)	Flaming area	m^2

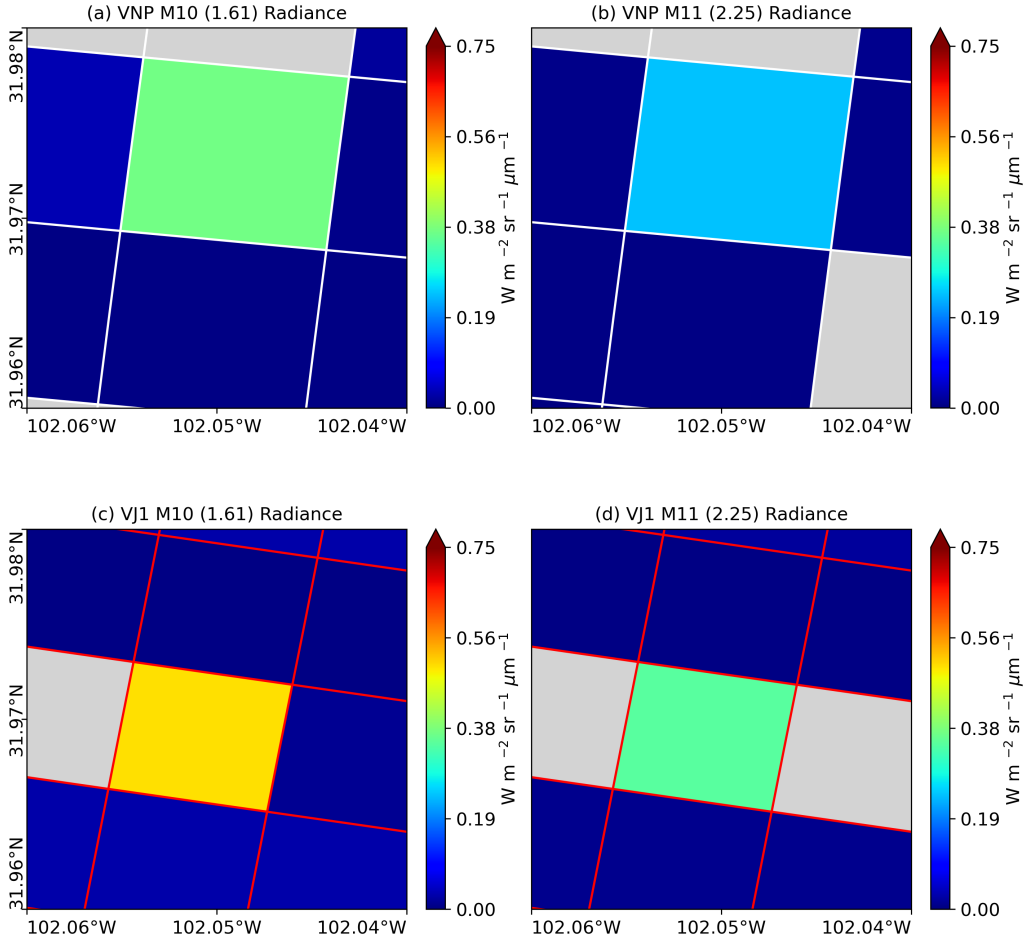

Figure A.17: Radiance measurements of the selected gas flaring case but from S-NPP at view zenith angle of 45°. (a) measured at S-NPP VIIRS 1.61 μm. (b) same as (a) but for VIIRS 2.25 μm. (c) and (d) are the Landsat observations in 1.6 μm and 2.2 μm. (c) and (d) are zoom in in different levels to provide a clear visualization. The white boxes on (a) and (b) are the VIIRS footprints in a resolution of ∼1000 m. The red boxes (c) and (d) show the LandSat footprint, in a spatial resolution of 30 meters.

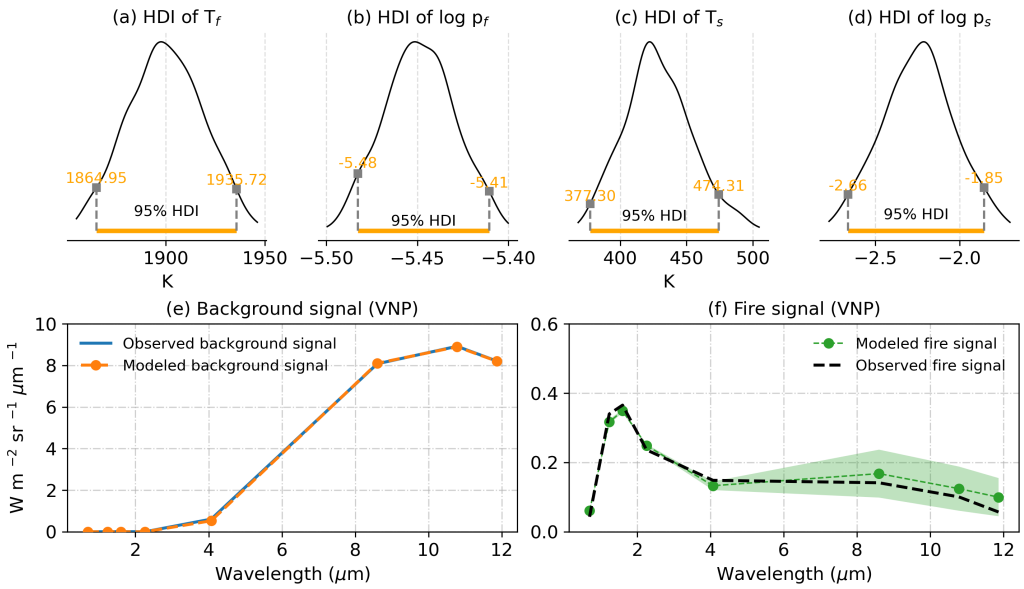

Figure A.18: HDI of the estimated fire parameters and reconstruct radiances of the selected case baed on the S-NPP VIIRS FILDA-2

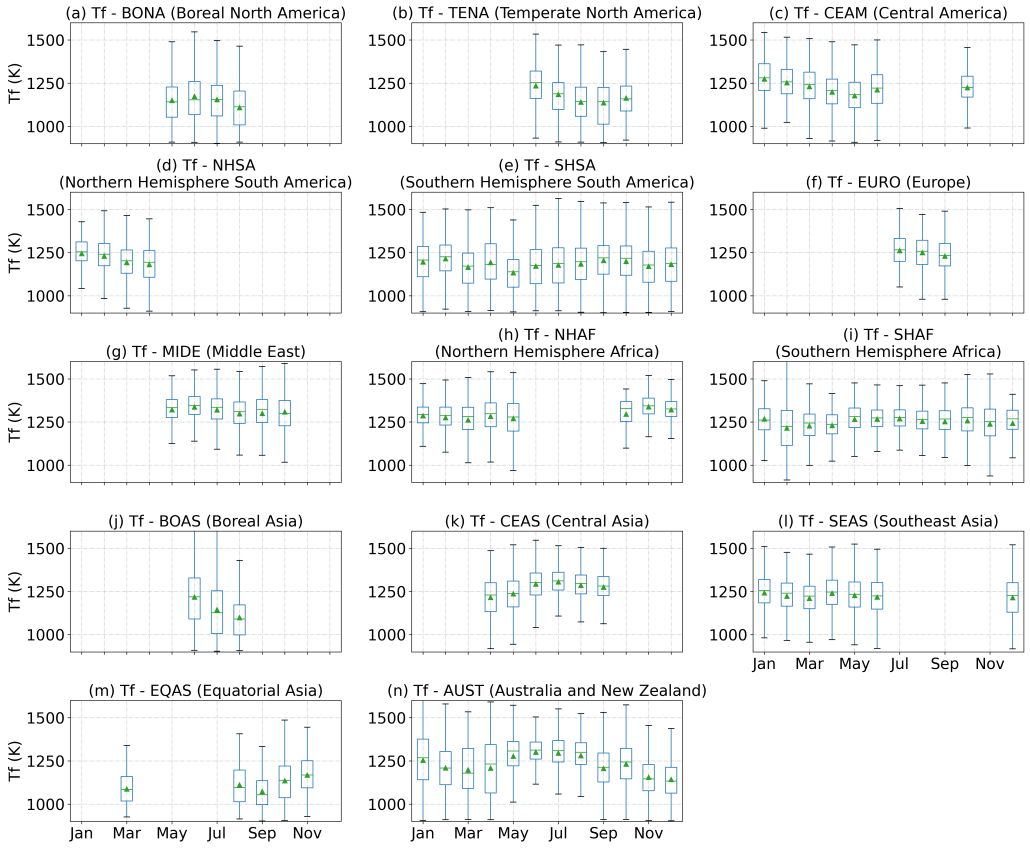

Figure A.19: Seasonal cycle of the flaming temperature over different regions based on GFED classification.

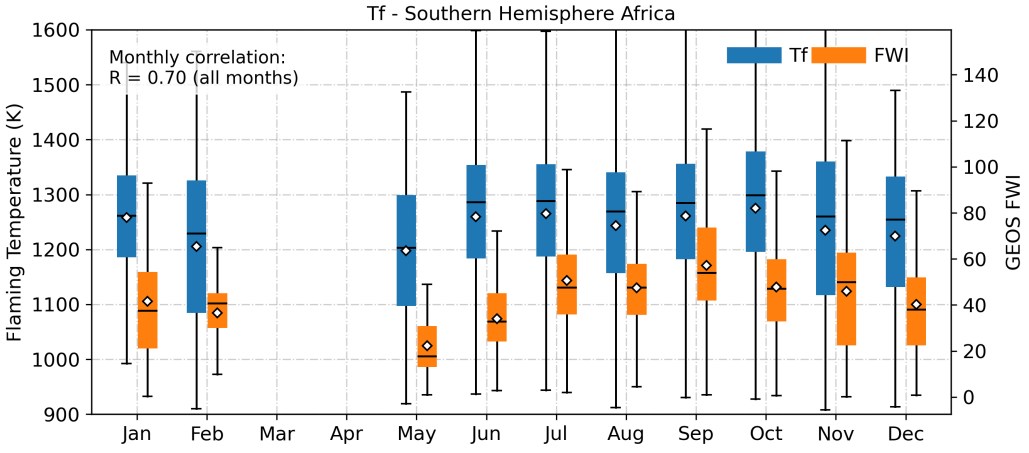

Figure A.20: Seasonal cycle of the flaming temperature and GEOS fire weather index for the grassland-like boime over Southern hemispheric Africa. Data in the tropical area are excluded to amply the seasonaly signal.

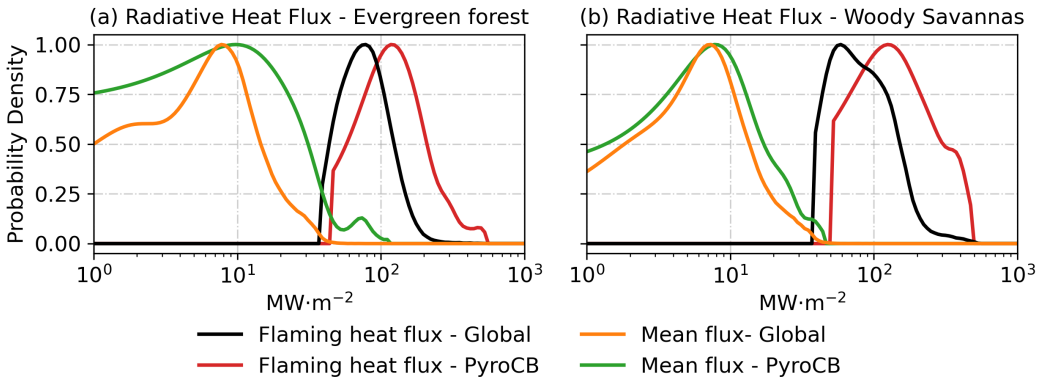

Figure A.21: Kernel density estimation for the radiative heat flux for the global and PyroCB events over evergreen forest and woody savannas. Black line is the flaming heat flux based on global fire events. Red line is the flaming heat flux over PyroCB events. Orange line is the mean heat flux based on global fire events. Green line is the mean heat flux over PyroCB events.

References

Oriol Abril-Pla, Virgile Andreani, Colin Carroll, Larry Dong, Christopher J Fonnesbeck, Maxim Kochurov, Ravin Kumar, Junpeng Lao, Christian C Luhmann, Osvaldo A Martin, et al. Pymc: a modern, and comprehensive probabilistic programming framework in python. *PeerJ Computer Science*, 9:e1516, 2023.

Martin E Alexander and WJ de Groot. Fire behavior in jack pine stands as related to the canadian forest fire weather index (fwi) system. 1988.

Tirtha Banerjee, Warren Heilman, Scott Goodrick, J Kevin Hiers, and Rod Linn. Effects of canopy midstory management and fuel moisture on wildfire behavior. *Scientific reports*, 10(1):17312, 2020.

Luca Carmignani, Mohammadhadi Hajilou, Jeanette Cobian-Iñiguez, Mark Finney, Scott L Stephens, Michael J Gollner, and Carlos Fernandez-Pello. Smoldering of wood: Effects of wind and fuel geometry. *Fire Technology*, 60(3):1667–1683, 2024.

A. Darmenov and A. M. da Silva. The Quick Fire Emissions Dataset (QFED): Documentation of versions 2.1, 2.2 and 2.4. *Technical Report Series on Global Modeling and Data Assimilation*, 38:1 – 212, 09 2015. URL https://gmao.gsfc.nasa.gov/pubs/docs/Darmenov796.pdf.

Weizhi Deng, Meng Zhou, Jun Wang, Zhixin Xue, Zhendong Lu, Xi Chen, Huanxin Zhang, David A Peterson, Edward J Hyer, and Arlindo M Da Silva. Advancing frp retrieval: Bridging theory and application. *IEEE Transactions on Geoscience and Remote Sensing*, 2024.

Jeff Dozier. A method for satellite identification of surface temperature fields of subpixel resolution. *Remote Sensing of environment*, 11:221–229, 1981.

TC Eckmann, DA Roberts, and CJ Still. Estimating subpixel fire sizes and temperatures from aster using multiple endmember spectral mixture analysis. *International Journal of Remote Sensing*, 30(22):5851–5864, 2009.

Christopher D Elvidge, Mikhail Zhizhin, Feng-Chi Hsu, and Kimberly E Baugh. Viirs nightfire: Satellite pyrometry at night. *Remote Sensing*, 5 (9):4423–4449, 2013.

Christopher D Elvidge, Mikhail Zhizhin, Kimberly Baugh, Feng-Chi Hsu, and Tilottama Ghosh. Methods for global survey of natural gas flaring from visible infrared imaging radiometer suite data. *Energies*, 9(1):14, 2015.

Saulo R Freitas, Karla M Longo, Robert Chatfield, D Latham, Maria Assunção Faus da Silva Dias, MO Andreae, E Prins, JC Santos, R Gielow, and JA Carvalho Jr. Including the sub-grid scale plume rise of vegetation fires in low resolution atmospheric transport models. *Atmospheric Chemistry and Physics*, 7(13):3385–3398, 2007.

Michael Fromm, René Servranckx, Brian J Stocks, and David A Peterson. Understanding the critical elements of the pyrocumulonimbus storm sparked by high-intensity wildland fire. *Communications Earth & Environment*, 3(1):243, 2022.

Andrew Gelman, John B Carlin, Hal S Stern, and Donald B Rubin. *Bayesian data analysis*. Chapman and Hall/CRC, 1995.

Louis Giglio and Jacqueline D Kendall. Application of the dozier retrieval to wildfire characterization: A sensitivity analysis. *Remote sensing of Environment*, 77(1):34–49, 2001.

Frank S Gilliam. Forest ecosystems of temperate climatic regions: from ancient use to climate change. *New Phytologist*, 212(4):871–887, 2016.

Chad Hoffman, Paulo Fernandes, Penelope Morgan, and Francisco Castro Rego. *Fire science: from chemistry to landscape management*. Springer, 2021.

Matthew D Hoffman, Andrew Gelman, et al. The no-u-turn sampler: adaptively setting path lengths in hamiltonian monte carlo. *J. Mach. Learn. Res.*, 15(1):1593–1623, 2014.

Tanvir Islam, Glynn C Hulley, Nabin K Malakar, Robert G Radocinski, Pierre C Guillevic, and Simon J Hook. A physics-based algorithm for the simultaneous retrieval of land surface temperature and emissivity from viirs thermal infrared data. *IEEE Transactions on Geoscience and Remote Sensing*, 55(1):563–576, 2016.

Rong Li, Minghui Tao, Meigen Zhang, Liangfu Chen, Lili Wang, Yi Wang, Xinjie He, Lifei Wei, Xin Mei, and Jun Wang. Application potential of satellite thermal anomaly products in updating industrial emission inventory of china. *Geophysical Research Letters*, 48(8):e2021GL092997, 2021.

W Timothy Liu, Kristina B Katsaros, and Joost A Businger. Bulk parameterization of air-sea exchanges of heat and water vapor including the molecular constraints at the interface. *Journal of Atmospheric sciences*, 36(9):1722–1735, 1979.

Yongxue Liu, Chuanmin Hu, Wenfeng Zhan, Chao Sun, Brock Murch, and Lei Ma. Identifying industrial heat sources using time-series of the viirs nightfire product with an object-oriented approach. *Remote Sensing of Environment*, 204:347–365, 2018.

E Louise Loudermilk, Joseph J O'Brien, Scott L Goodrick, Rodman R Linn, Nicholas S Skowronski, and J Kevin Hiers. Vegetation's influence on fire behavior goes beyond just being fuel. *Fire Ecology*, 18(1):9, 2022.

RA McClatchey. *Optical properties of the atmosphere*. Number 411. Air Force Cambridge Research Laboratories, Office of Aerospace Research . . . , 1972.

Oleg M Melnik, Stephen A Paskaluk, Mark Y Ackerman, Katharine O Melnik, Dan K Thompson, Sara S McAllister, and Mike D Flannigan. New in-flame flammability testing method applied to monitor seasonal changes in live fuel. *Fire*, 5(1):1, 2021.

WP Menzel, EC Cutrim, and EM Prins. Geostationary satellite estimation of biomass burning in amazonia during base-a, global biomass burning (js levine, ed), 1991.

Steven D Miller, William Straka III, Stephen P Mills, Christopher D Elvidge, Thomas F Lee, Jeremy Solbrig, Andi Walther, Andrew K Heidinger, and Stephanie C Weiss. Illuminating the capabilities of the suomi national polar-orbiting partnership (npp) visible infrared imaging radiometer suite (viirs) day/night band. *Remote Sensing*, 5(12):6717–6766, 2013.

EJ Mlawer, VH Payne, JL Moncet, JS Delamere, MJ Alvarado, and DC Tobin. Development and recent evaluation of the mt_ckd model of continuum absorption, philos. Technical report, TR Soc. A, 370, 2520–2556, https://doi. org/10.1098/rsta, 2012.

Patricia Oliva and Wilfrid Schroeder. Assessment of viirs 375 m active fire detection product for direct burned area mapping. *Remote Sensing of Environment*, 160:144–155, 2015.

David Peterson and Jun Wang. A sub-pixel-based calculation of fire radiative power from modis observations: 2. sensitivity analysis and potential fire weather application. *Remote Sensing of Environment*, 129:231–249, 2013.

David Peterson, Jun Wang, Charles Ichoku, Edward Hyer, and Vincent Ambrosia. A sub-pixel-based calculation of fire radiative power from modis observations: 1: Algorithm development and initial assessment. *Remote Sensing of Environment*, 129:262–279, 2013.

David Peterson, Edward Hyer, and Jun Wang. Quantifying the potential for high-altitude smoke injection in the north american boreal forest using the standard modis fire products and subpixel-based methods. *Journal of Geophysical Research: Atmospheres*, 119(6):3401–3419, 2014.

David A Peterson, Melinda T Berman, Michael D Fromm, René Servranckx, William J Julstrom, Edward J Hyer, James R Campbell, Theodore M McHardy, and Andrew Lambert. Worldwide inventory reveals the frequency and variability of pyrocumulonimbus and stratospheric smoke plumes during 2013–2023. *npj Climate and Atmospheric Science*, 8(1): 325, 2025.

Thomas N Polivka, Edward J Hyer, Jun Wang, and David A Peterson. First global analysis of saturation artifacts in the viirs infrared channels and the effects of sample aggregation. *IEEE Geoscience and Remote Sensing Letters*, 12(6):1262–1266, 2015.

Derek J Posselt. Markov chain monte carlo methods: Theory and applications. In *Data Assimilation for Atmospheric, Oceanic and Hydrologic Applications (Vol. II)*, pages 59–87. Springer, 2013.

Guillermo Rein. Smoldering combustion. *SFPE handbook of fire protection engineering*, pages 581–603, 2016.

Laurence S Rothman, Iouli E Gordon, Yury Babikov, Alain Barbe, D Chris Benner, Peter F Bernath, Manfred Birk, Luca Bizzocchi, Vincent Boudon, Linda R Brown, et al. The hitran2012 molecular spectroscopic database.

Journal of Quantitative Spectroscopy and Radiative Transfer, 130:4–50, 2013.

John Salvatier, Thomas V Wiecki, and Christopher Fonnesbeck. Probabilistic programming in python using pymc3. *PeerJ Computer Science*, 2:e55, 2016.

Wilfrid Schroeder, Patricia Oliva, Louis Giglio, and Ivan A Csiszar. The new viirs 375 m active fire detection data product: Algorithm description and initial assessment. *Remote Sensing of Environment*, 143:85–96, 2014.

Carl F Schueler, John E Clement, Philip E Ardanuy, Carol Welsch, Frank DeLuccia, and Hilmer Swenson. Npoess viirs sensor design overview. In *Earth Observing Systems VI*, volume 4483, pages 11–23. SPIE, 2002.

Maria Val Martin, Ralph A Kahn, Jennifer A Logan, Ronan Paugam, Martin Wooster, and Charles Ichoku. Space-based observational constraints for 1-d fire smoke plume-rise models. *Journal of Geophysical Research: Atmospheres*, 117(D22), 2012.

Oswald Wallner, Thido Reinert, and Christoph Straif. Metimage: a spectroradiometer for the vii mission onboard metop-sg. In *International Conference on Space Optics—ICSO 2016*, volume 10562, pages 107–114. SPIE, 2017.

Jun Wang, Xiaoguang Xu, Shouguo Ding, Jing Zeng, Robert Spurr, Xiong Liu, Kelly Chance, and Michael Mishchenko. A numerical testbed for remote sensing of aerosols, and its demonstration for evaluating retrieval synergy from a geostationary satellite constellation of geo-cape and goes-r. *Journal of Quantitative Spectroscopy and Radiative Transfer*, 146:510–528, 2014.

Jun Wang, Sepehr Roudini, Edward J Hyer, Xiaoguang Xu, Meng Zhou, Lorena Castro Garcia, Jeffrey S Reid, David A Peterson, and Arlindo M Da Silva. Detecting nighttime fire combustion phase by hybrid application of visible and infrared radiation from suomi npp viirs. *Remote sensing of environment*, 237:111466, 2020a.

Jun Wang, Meng Zhou, Xiaoguang Xu, Sepehr Roudini, Stanley P Sander, Thomas J Pongetti, Steven D Miller, Jeffrey S Reid, Edward Hyer, and

Robert Spurr. Development of a nighttime shortwave radiative transfer model for remote sensing of nocturnal aerosols and fires from viirs. *Remote sensing of environment*, 241:111727, 2020b.

D Ward. Combustion chemistry and smoke. In *Forest fires*, pages 55–77. Elsevier, 2001.

Martin J Wooster, Weidong Xu, and T Nightingale. Sentinel-3 slstr active fire detection and frp product: Pre-launch algorithm development and performance evaluation using modis and aster datasets. *Remote sensing of environment*, 120:236–254, 2012.

MJ Wooster, B Zhukov, and D Oertel. Fire radiative energy for quantitative study of biomass burning: Derivation from the bird experimental satellite and comparison to modis fire products. *Remote Sensing of Environment*, 86(1):83–107, 2003.

Xiaoxiong Xiong, James Butler, Kwofu Chiang, Boryana Efremova, Jon Fulbright, Ning Lei, Jeff McIntire, Hassan Oudrari, Junqiang Sun, Zhipeng Wang, et al. Viirs on-orbit calibration methodology and performance. *Journal of Geophysical Research: Atmospheres*, 119(9):5065–5078, 2014.

Xiaoxiong Xiong, Amit Angal, James Butler, Hongda Chen, Kwofu Chiang, Ning Lei, Yonghong Li, and Kevin Twedt. Performance assessments and comparisons of s-npp and noaa-20 (jpss-1) viirs on-orbit calibration. In *Sensors, Systems, and Next-Generation Satellites XXII*, volume 10785, pages 192–204. SPIE, 2018.

Meng Zhou, Jun Wang, Xi Chen, Xiaoguang Xu, Peter R Colarco, Steven D Miller, Jeffrey S Reid, Shobha Kondragunta, David Matthew Giles, and Brent Holben. Nighttime smoke aerosol optical depth over us rural areas: First retrieval from viirs moonlight observations. *Remote Sensing of Environment*, 267:112717, 2021.

Meng Zhou, Jun Wang, Lorena Castro Garcia, Xi Chen, Arlindo M da Silva, Zhuosen Wang, Miguel O Román, Edward J Hyer, and Steven D Miller. Enhancement of nighttime fire detection and combustion efficiency characterization using suomi-npp and noaa-20 viirs instruments. *IEEE Transactions on Geoscience and Remote Sensing*, 61:1–20, 2023.

Meng Zhou, Jun Wang, Xi Chen, Yi Wang, Peter R Colarco, Robert C Levy, and Steven D Miller. First lunar-light mapping of nighttime dust season oceanic aerosol optical depth over north atlantic from space. *Remote sensing of environment*, 312:114315, 2024.

Meng Zhou, Arlindo M. da Silva, Jun Wang, and David A. Peterson. Montecarlo biphasic estimation of fire properties (mcbef): Part i, algorithm formulation. *Remote Sensing of Environment*, 2026. submitted.

Ciyou Zhu, Richard H Byrd, Peihuang Lu, and Jorge Nocedal. Algorithm 778: L-bfgs-b: Fortran subroutines for large-scale bound-constrained optimization. *ACM Transactions on mathematical software (TOMS)*, 23(4): 550–560, 1997.